Geol. Mag. **155** (*4*), *2018, pp. 955–978.* *© Cambridge University Press 2017*
doi:10.1017/S0016756816001242

Metamorphic evolution of Palaeoproterozoic anatectic migmatites in the eastern part of the Aravalli–Delhi Fold Belt, India: constraints from thermodynamic modelling and monazite dating

A. PRAKASH*, L. SAHA*†, I. PETRIK‡, M. JANAK‡ & A. BHATTACHARYA§

*Department of Earth Sciences, Indian Institute of Technology Roorkee, 247667 Roorkee, India
‡Earth Science Institute of the Slovak Academy of Sciences, 84005 Bratislava, Slovak Republic
§Department of Geology and Geophysics, Indian Institute of Technology Kharagpur, 721302 Kharagpur, India

(*Received* 16 June 2016; *accepted* 12 December 2016; *first published online* 6 March 2017)

Abstract – Garnetiferous pelitic to psammopelitic migmatites widespread across the central and eastern part of the Aravalli–Delhi Fold Belt in NW India record two distinct orogenies, e.g. the Aravalli Orogeny (1.7–1.6 Ga) and the Delhi Orogeny (1.0 Ga). In this study, we integrate field geological studies with textural and mineral–chemical analyses, P–T pseudosection modelling and *in situ* monazite dating in anatectic migmatites in the Aravalli Supergroup occurring along the Deoli–Shahpura segment. The study reveals formation of peak assemblages of garnet + sillimanite + biotite + K-feldspar + melt and garnet + muscovite + K-feldspar + melt in two anatectic migmatite samples. P–T pseudosection modelling suggests that anatexis in the gneisses occurred at ~8 kbar and 700–800 °C along a tight-loop clockwise P–T path. Monazite ages from the migmatites indicate that the anatexis occurred at ~1.73–1.74 Ga. This age is similar to the Palaeoproterozoic anatexis (at 7–8 kbar) and charnockite emplacement in the Sandmata and the Mangalwar complexes, the subsolidus amphibolite-facies metamorphism in the Rajpura–Dariba and Pur–Banera supracrustal belts, and the A-type granite magmatism in the North Delhi Fold Belt. We propose that the Palaeoproterozoic migmatites in central and eastern Rajasthan are part of the one crustal unit that underwent anatexis during an accretion event along the NE–SW-trending Aravalli orogenic belt.

Keywords: Aravalli–Delhi Fold Belt, Aravalli Supergroup, Proterozoic orogeny, Deoli–Shahpura migmatites, anatexis, pseudosection, monazite ages

1. Introduction

The Aravalli–Delhi Fold Belt (ADFB) in NW India preserves a record of a protracted period of crustal evolution spanning from ~3.3 Ga to 1.0 Ga (Fig. 1a; Crawford & Compston, 1970; Sivaram & Odom, 1982; MacDougall *et al.* 1983; Choudhary, Gopalan & Sastry, 1984; Sarkar, Barman & Corfu, 1989; Volpe & Mcdougall, 1990; Gopalan *et al.* 1990; Sastry, 1992; Guha & Garkhal, 1993; Goswami, Wiedenbeck & Roy, 1994; Tobisch *et al.* 1994; Wiedenbeck & Goswami, 1994; Sharma, 1995; Lopez *et al.* 1996; Wiedenbeck, Goswami & Roy, 1996*a*,*b*; Roy & Kröner, 1996; Fareeduddin & Kröner, 1998; Mukhopadhay *et al.* 2000; Deb & Thorpe, 2004; Roy *et al.* 2005, 2012; Buick *et al.* 2006, 2010; Kaur *et al.* 2006, 2007, 2011*a*,*b*; Bhowmik, Bernhardt & Dasgupta, 2010). The NNE-trending polymetamorphic ADFB sandwiched between the Marwar Craton in the west and the Meso/Neoarchaean Bundelkhand Craton in the east records two major orogenies, i.e. (i) the 1.8–1.7 Ga Aravalli Orogeny and the (ii) Grenvillian-age Delhi Orogeny (Volpe & Mcdougall, 1990; Kaur *et al.* 2006, 2007, 2011*a*,*b*; Buick *et al.* 2006, 2010; Bhowmik, Bernhardt & Dasgupta, 2010). The Palaeoproterozoic Aravalli Orogeny is marked by (i) the emplacement of rift-related A-type granitoids around Khetri and Jasrapura in the North Delhi Fold Belt (NDFB; Kaur *et al.* 2007, 2009, 2011*a*), (ii) mid-crustal amphibolite-facies metamorphism of the Rajpura–Dariba and the Pur–Banera schist belts (Hazarika, Upadhyay & Mishra, 2013; Ozha *et al.* 2016) and (iii) sillimanite-facies crustal anatexis along the NE–SW-trending Sandmata Complex (SC) and Mangalwar Complex (MC, constituting BGC-II; Heron, 1953; Buick *et al.* 2006, 2010; Saha *et al.* 2008; Bhowmik, Bernhardt & Dasgupta, 2010; Roy *et al.* 2012). Besides, detrital zircons from the Alwar quartzite unit (the oldest stratigraphic unit in the NDFB) and the greenschist-facies schists of the Aravalli Supergroup around Jhamarkotra (Fig. 1b) yield ages of ~1.8–1.7 Ga (Kaur *et al.* 2011*b*; McKenzie *et al.* 2013). These sedimentary successions are believed to have formed in rift-related basins under extensional tectonic regimes (Kaur *et al.* 2011*b*; McKenzie *et al.* 2013). Earlier tectonic models proposed for crustal evolution of the ADFB include the (i) two Wilson cycles model of Sinha-Roy (1988) and Vijaya Rao *et al.* (2000), (ii) one Wilson cycle model of Sugden, Deb & Windley (1990), (iii) ensialic orogenesis by Roy (1990) and Sharma (1995), and

---

†Author for correspondence: saha.lopamudra@gmail.com

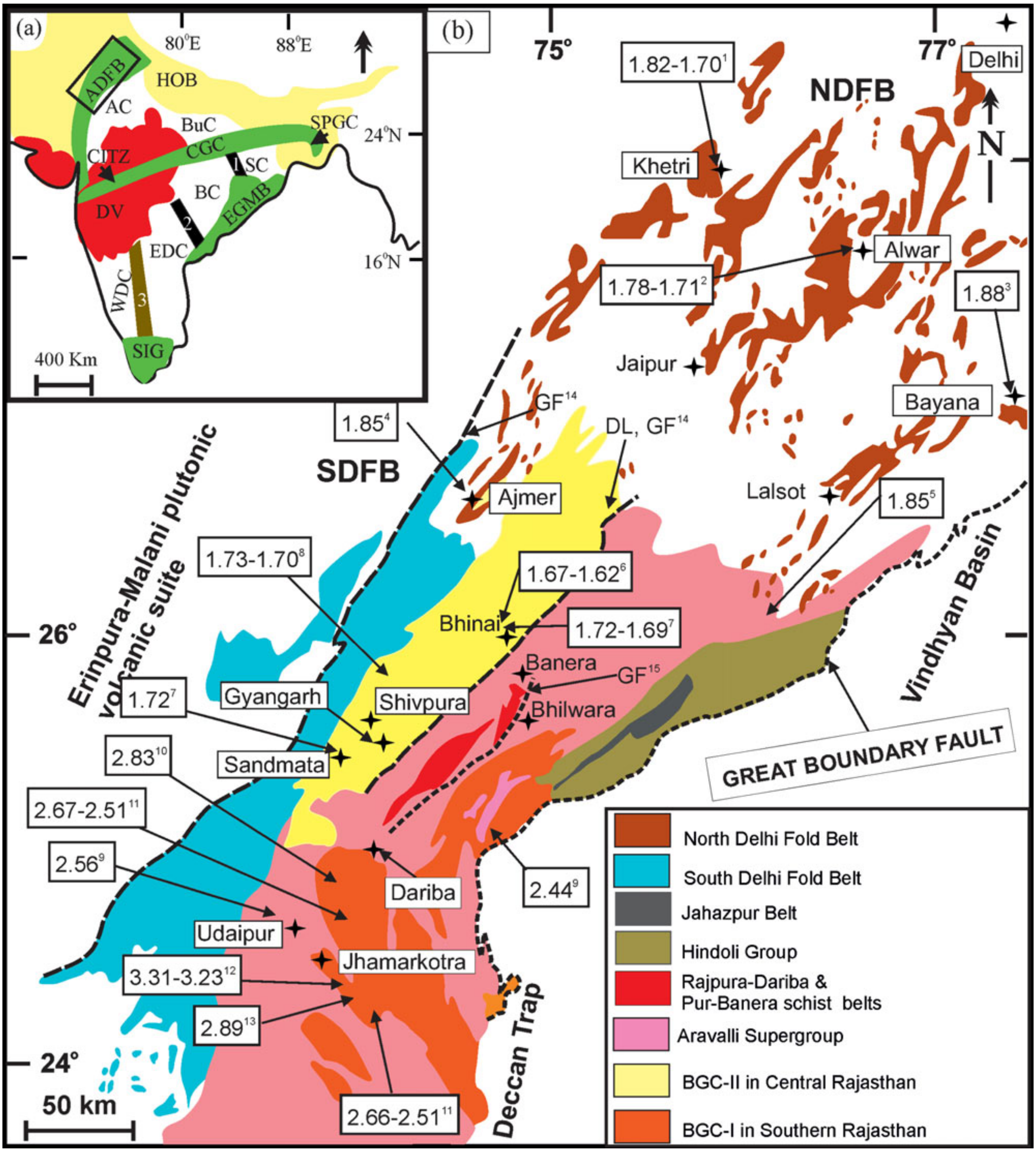

Figure 1. (Colour online) (a) General tectonic map of Peninsular India (modified after Radhakrishna, 1989) showing the location of Archaean cratons and Proterozoic mobile belts. Abbreviations: ADFB – Aravalli–Delhi Fold Belt; AC – Aravalli Craton; BuC – Bundelkhand Craton; SC – Singhbhum Craton; BC – Bastar Craton; EDC – Eastern Dharwar Craton; WDC – Western Dharwar Craton; CITZ – Central Indian Tectonic Zone; CGC – Chotanagpur Gneissic Complex; SPGC – Shillong Plateau Gneissic Complex; EGMB – Eastern Ghats Mobile Belt; SIG – South Indian Granulite terrain; HOB – Himalayan Orogenic Belt; DV – Deccan Volcanics; 1 – Mahandi Rift; 2 – Godavari Rift; 3 – Closepet Granite. Study area in the ADFB is shown in the box. (b) Geological map of Aravalli–Delhi Fold Belt, NW India (modified after Roy, 1988; Roy & Jakhar, 2002) showing ages of important events. Age data sources: 1 – Deb & Sarkar (1990), Kaur *et al.* (2007, 2009, 2011); 2 – Biju-Sekhar *et al.* (2003); 3 – Deb & Thorpe (2004); 4 – Mukhopadhyay *et al.* (2000); 5 – Deb, Thorpe & Krstic (2002); 6 – Roy *et al.* (2005); 7 – Buick *et al.* (2006); 8 – Sarkar, Barman & Corfu (1989), Fareeduddin & Kröner (1998), Bhowmik, Bernhardt & Dasgupta (2010); 9 – Wiedenbeck, Goswami & Roy (1996*a*); 10 –Gopalan *et al.* (1990); 11 – Wiedenbeck, Goswami & Roy (1996*b*), Roy & Kröner (1996); 12 – Gopalan *et al.* (1990), Wiedenbeck & Goswami (1994), Roy & Kröner (1996); 13 – Roy & Kröner (1996); 14 – Bhowmik, Bernhardt & Dasgupta (2010); 15 – Ozha *et al.* (2016). Abbreviation: BGC – Banded Gneissic Complex. BGC-I and BGC-II after Heron (1953), respectively, include the Archaean gneissic terrain and the central gneissic terrain.

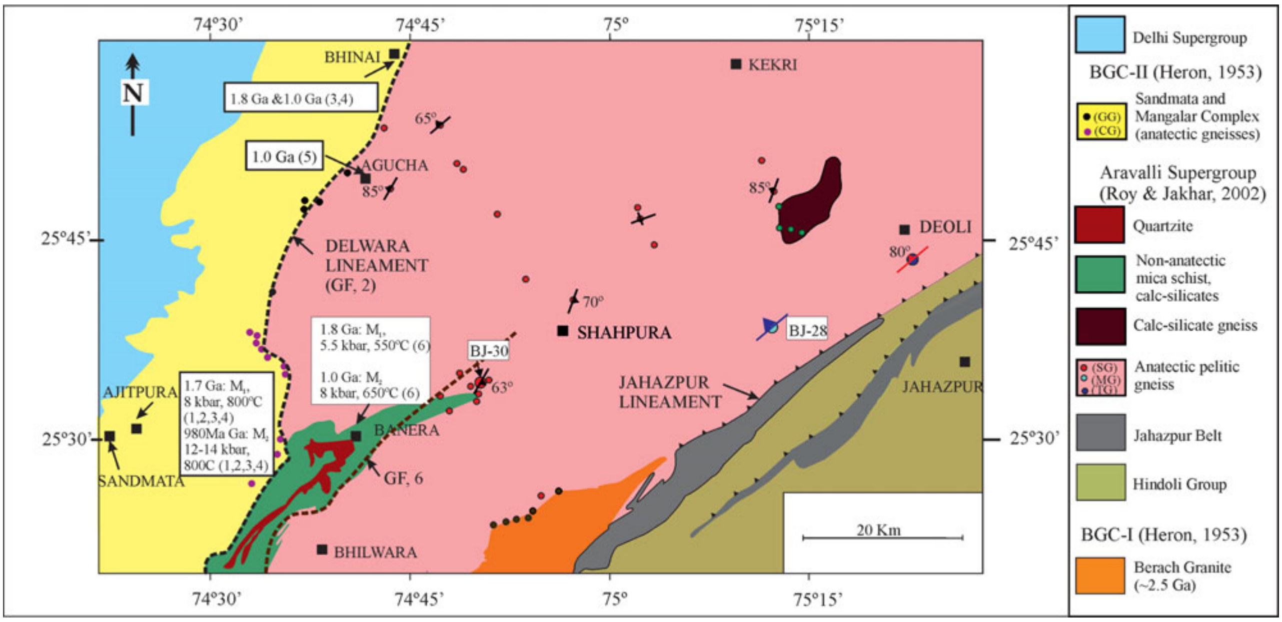

Figure 2. (Colour online) Geological map of the central and eastern Aravalli–Delhi Fold Belt (modified after Geological Survey of India quadrangle maps) showing lithology, sample locations (along different transects) and pervasive foliation data. Abbreviations: GF – Grenvillian Front; GG – granite gneiss; CG – calc-silicate gneiss; SG – garnet–biotite–sillimanite gneiss; MG – muscovite gneiss; TG – tourmaline–muscovite gneiss. Delhi Supergroup on this map is the stratigraphic name for the South Delhi Fold Belt shown in Figure 1.

(iv) inversion tectonics by Verma & Greiling (1995). Bhowmik & Dasgupta (2012) proposed that rift-related granite magmatism and sedimentation in the NDFB and crustal anatexis in the SC and MC occurred as a result of switching between subduction and extensional tectonics (in back-arc settings) during the Palaeoproterozoic Aravalli Orogeny.

Reworking of the ∼1.8–1.7 Ga gneissic crust in the SC and MC occurred at ∼12–14 kbar pressures and >750 °C as a result of collisional tectonics during the Grenvillian Delhi Orogeny (Buick *et al.* 2006, 2010; Bhowmik, Bernhardt & Dasgupta, 2010; Bhowmik & Dasgupta, 2012). The studies are based on the anatectic high-grade SC and the Rampura–Agucha anatexites in the MC, the non-anatectic amphibolite-facies Rajpura–Dariba and Pur–Banera schist belts, and the granitoids of the NDFB and SDFB (Fig. 1b). However, the metamorphic evolutionary history of the vast swathes of anatectic migmatites exposed, albeit poorly, eastwards of the Rampura–Agucha anatexites and the non-anatectic schists of the Pur–Banera, and extending up to the Hindoli Supergroup rocks in the east and the Archaean Berach granite (Fig. 2) remain largely unknown. Naha & Roy (1983) suggested the mesoscale structures in these anatectic migmatites are similar to the ones in the Sandmata and the Mangalwar complexes. Roy & Jakhar (2002) considered these gneisses to be the high-grade equivalents of rocks in the Aravalli Supergroup. However, in the absence of metamorphic characterization and geochronology in these anatectic migmatites, the relevance of these migmatites in the Proterozoic crustal evolution history of the Aravalli craton remains speculative. In this study based on field geological studies, P–T estimation obtained using thermodynamic modelling of reaction equilibria and monazite dating, we address if these anatectic migmatites shared the polycyclic history recorded in the SC and MC migmatites. A consequence of this study is to examine the eastward extent of Grenvillian-age tectonism along the intensely tectonized Delwara Lineament formed owing to the welding of the MC with the SC in the west.

2. Geological setting

The Aravalli Supergroup of rocks in the Bhilwara Sector are distributed along two NE–SW-trending subparallel belts: (i) an eastern belt consisting of the low-grade volcano-sedimentary units of the Hindoli Group, and (ii) a western belt consisting of the amphibolite-facies mica schist–quartzite sequence of the Rajpura–Dariba and Pur–Banera schist belts in the south and migmatites in the north (Fig. 2), whose stratigraphic relationships are not established owing to lack of geochronological data. The eastern low-grade belt is separated from the Vindhyan Supergroup of rocks in the east by the Great Boundary Fault and from the migmatite belt in the west by the Jahazpur lineament (Fig. 2; Gupta *et al.* 1980; Sinha-Roy, Malhotra & Mohanty, 1998; Verma, 1999). The Jahazpur lineament has been identified as a thrust belt comprising the amphibolite-facies lithologies of the Jahazpur Belt along the northern margin of the low-grade metamorphic rocks of the Hindoli Group (Sinha-Roy & Malhotra, 1989; Tiwari *et al.* 1998). The low-grade units of the Hindoli Group form a volcano-sedimentary succession comprising interlayered quartzite, pelite, carbonates, lava flows and tuffs of both felsic and mafic volcanic rocks (Gupta *et al.* 1980; Bose & Sharma, 1992).The mica schist–quartzite sequence in the southern part of the western belt forms a NE–SW-trending folded belt extending from the Rajpura–Dariba in the southwest to Pur–Banera in the northeast (Fig. 2; Hazarika, Upadhyay & Mishra, 2013; Ozha *et al.* 2016). Mica schists from the belt comprise a garnet–biotite–muscovite–kyanite–quartz–feldspar–chlorite assemblage (Hazarika, Upadhyay & Mishra, 2013; Ozha *et al.* 2016).

In the course of this study along transects across the anatectic migmatites of the Bhilwara Sector (Fig. 2), garnet–biotite–sillimanite gneisses appear to be the most dominant lithologies, albeit poorly exposed, extending from Bhilwara in the southwest, Agucha in the northwest, and Kekri and Deoli in the arc between the northeast and southeast, respectively (Figs 1b, 2). These migmatites are locally interleaved with amphibolites and calc-silicate gneisses and intruded by variably deformed porphyritic granites (this study; Roy, Somani & Sharma, 1981; A. B. Roy, Hindusthan Zinc Ltd, unpub. project report, 2000). Lithological variations are best observed along the Deoli–Shahpura transect (Fig. 2). Along this transect, outcrops of anatectic migmatites were observed at two localities at Deoli, BJ-28 (25° 38.301′ N, 75° 6.879′ E) and BJ-30 (25° 34.162′ N, 74° 50.087′ E; Fig. 2). The migmatite near Deoli occurs at the contact of the phyllite–quartzite-carbonates of the Jahazpur thrust belt. The gneissic banding in the migmatite is defined by muscovite–biotite–tourmaline-bearing mesocratic bands alternating with quartz–feldspar–tourmaline-bearing leucocratic bands (Fig. 3a). At ~22 km SW, small scattered outcrops of muscovite–biotite–garnet-bearing migmatite (BJ-28) occur (Fig. 3b). The migmatite layering in these rocks is composed of garnet–muscovite–biotite-bearing mesocratic bands and quartz–feldspar-bearing leucocratic bands. The first outcrop of biotite–garnet–sillimanite–feldspar-bearing gneiss (BJ-30) occurs about 40 km SW of BJ-28, near Shahpura (Fig. 2). At this locality, the migmatitic banding is formed by garnet–biotite–sillimanite–quartz-bearing mesocratic bands and quartz–feldspar-bearing leucocratic bands (Fig. 3c). We have chosen these two anatectic migmatite samples (BJ-28 and BJ-30) to understand the spatial variations, if any, in *P–T* conditions of anatexis in the two localities, or whether bulk compositional variations were responsible for muscovite melting and biotite melting in the two localities. Monazite age dating was carried out on these samples to determine if partial melting in both localities was coeval or not.

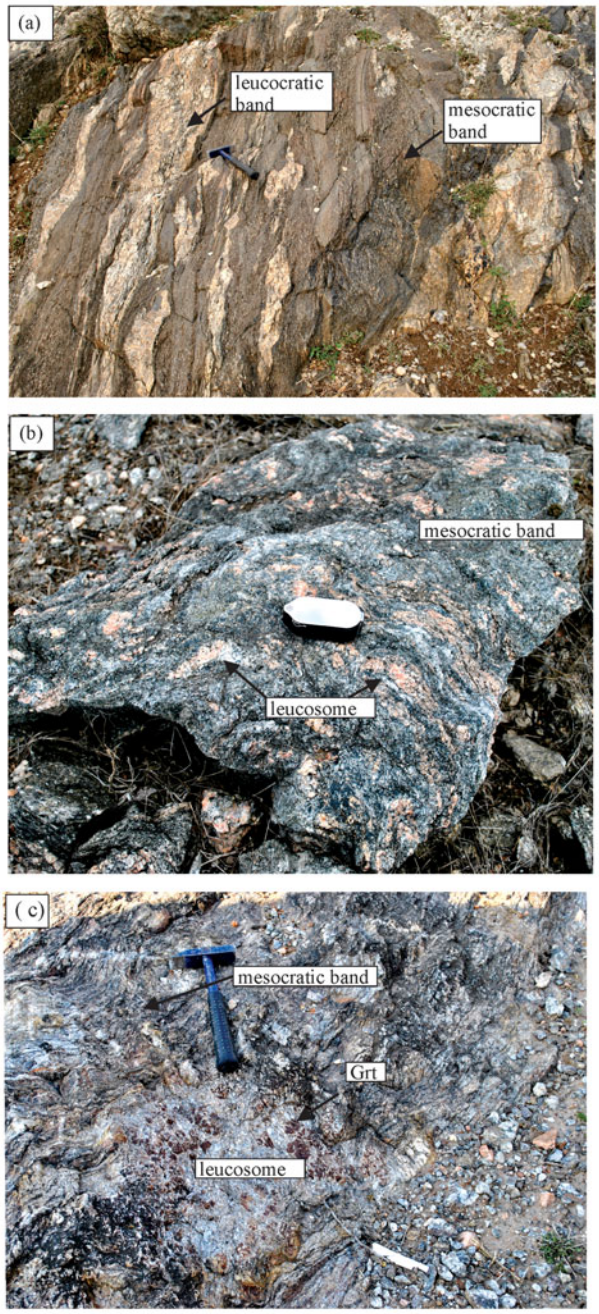

Figure 3. (Colour online) Field photographs showing migmatitic bandings in (a) tourmaline-bearing muscovite gneiss occurring around Deoli, (b) garnet–muscovite–biotite-bearing gneiss (BJ-28) and (c) field photograph of garnet–biotite–sillimanite–feldspar-bearing gneiss (BJ-30). Mineral abbreviations used in this figure are after Kretz (1983). Same abbreviations are also used for other figures and tables. Hammer for scale is 38 cm long; hand lens for scale is 4.5 cm long.

3. Results

3.a. Petrography and mineral chemistry

3.a.1. Garnet–muscovite–biotite gneiss (BJ-28)

The mesocratic domain in the sample comprises garnet, muscovite, biotite and quartz (Fig. 4a). Garnet porphyroblasts contain inclusion trails (S_i) of quartz and biotite. Pervasive foliation in the matrix (S_e) is formed by oriented muscovite and biotite (Fig. 4a). Inclusion trails (S_i) in garnet porphyroblasts occur at a high angle with respect to the matrix foliation. Coarse muscovite grains overgrow matrix foliation (Fig. 4b). Leucocratic domains consist mainly of quartz and K-feldspar, and minor plagioclase. Foliation formed by muscovite wraps around a coarse K-feldspar in the

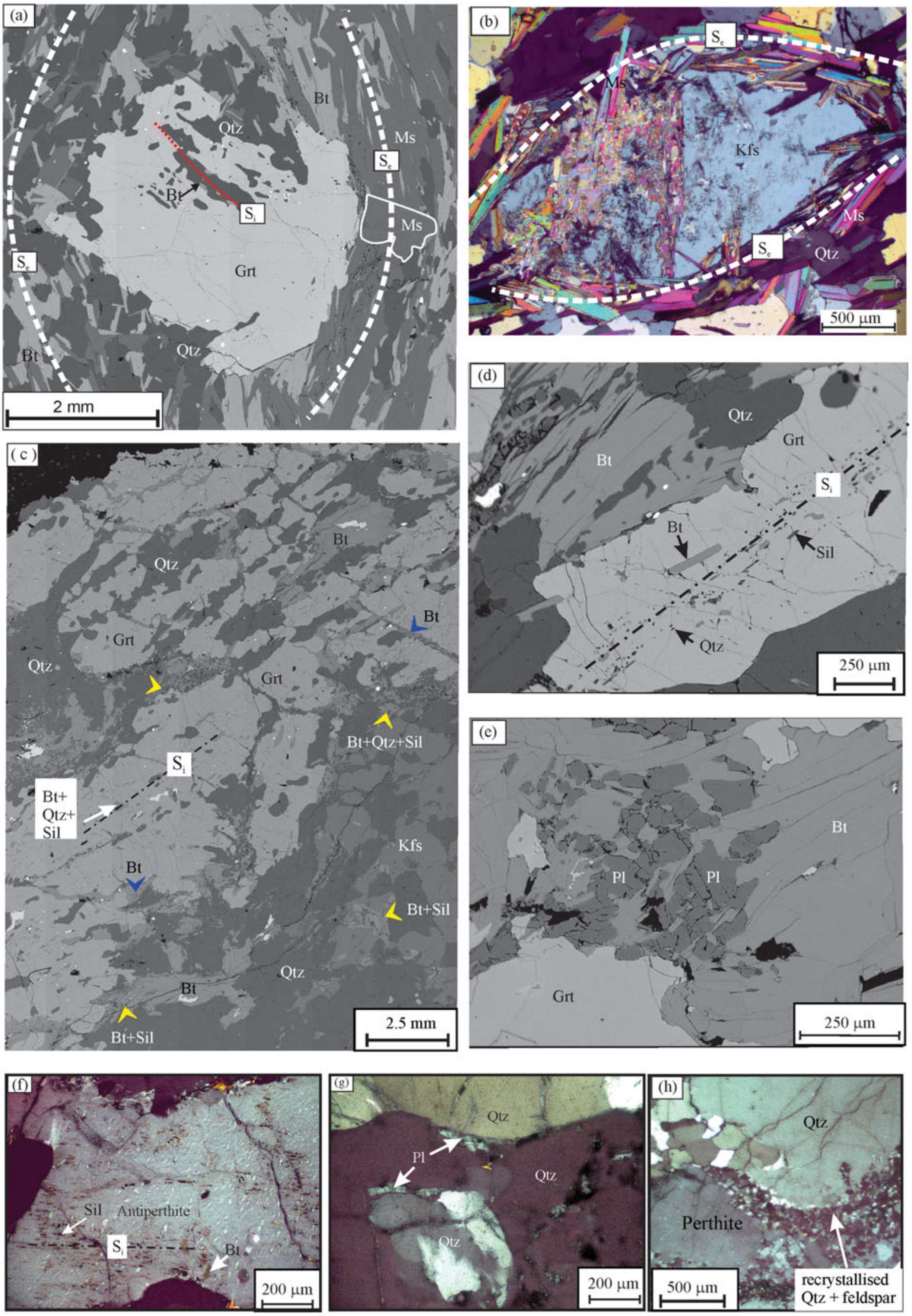

Figure 4. (Colour online) (a) BSE image of mesocratic band of BJ-28 in which inclusion trails in garnet (S_i) are formed by biotite + quartz and S_e marks the pervasive foliation in the matrix formed by biotite + muscovite + quartz. (b) Thin-section photograph of leucocratic band of BJ-28 showing a coarse potash feldspar grain wrapped around by muscovite forming foliation S_e. (c, d) BSE images of BJ-30 showing presence of garnet + biotite + sillimanite + feldspar in the mesocratic band (c & d) and quartz–potash

leucosome (Fig. 4b). Overgrowths of muscovite on the foliation and replacement of feldspar by muscovite are also common. Microstructural observations like inclusions of biotite and quartz in the garnet porphyroblasts indicate breakdown of biotite and quartz during garnet formation (Fig. 4a). Additionally, the presence of muscovite in the leucocratic bands indicates participation of muscovite in the following partial melting reaction:

$$\text{biotite} + \text{muscovite} + \text{quartz} + \text{plagioclase} \rightarrow \text{garnet} + \text{K} - \text{feldspar} + \text{melt} \qquad (1)$$

Muscovite-defined foliation wrapping around garnet porphyroblasts in the mesocratic bands and coarse K-feldspars in the leucocratic bands indicate that formation of the foliation post to melting and replacement of K-feldspar by muscovite is due to retrogression.

Garnet porphyroblasts are mostly solid solutions of pyrope and almandine with minor grossular and spessartine contents (Table 1a; analytical methods are given in the Appendix). Two sets of data from core to rims (marked as profile 1 and 2 in Table 1a) of a garnet porphyroblast indicate compositional homogeneity from core (away from any biotite inclusion) to the outer rims ($Alm_{0.81–0.82}Prp_{0.11–0.10}Grs_{0.04–0.03}Sps_{0.05–0.04}$ and X_{Mg} ~0.12–0.11) with pyrope contents decreasing significantly at the edge of the garnet (X_{Prp} ~0.08) against matrix biotite (Table 1a). X_{Mg} of the garnet edge at the contact with matrix biotite is ~0.08–0.09, which is ~2–3 mol.% lower than that in the garnet core. On the contrary, compositions of the garnet core at the contacts with biotite inclusions are similar to those at the edges of the garnet against matrix biotite (Table 1a). X_{Mg} values of matrix biotite show no significant variation from cores (~0.34–0.37) to rims (~0.34–0.36; Table 1a). Titanium contents of the individual matrix biotite grains do not show any variation from their cores (~1.672–1.738 apfu based on 11 O) to rims (~1.689–1.723 apfu based on 11 O; Table 1a). X_{Mg} values of the biotite inclusions in garnet porphyroblasts (~0.43–0.46) are higher than those of the matrix biotite porphyroblasts (Table 1b). Titanium contents of the biotite inclusions vary from 0.135 to 0.156 (Table 1a). Si contents of muscovite grains from the foliation domains vary from 3.085–3.132 apfu (based on 11 O), their total aluminium contents varying from 2.640–2.768 apfu (based on 11 O; Table 1a).

3.a.2. Garnet–biotite–sillimanite gneiss (BJ-30)

The sample consists of garnet, biotite, sillimanite, quartz and feldspars (Fig. 4c). Garnet porphyroblasts are elongated, with inclusion trails formed by oriented biotite–sillimanite and globular quartz grains (Figs 4c–d). Leucocratic bands consist of plagioclase–K-feldspar, quartz and sillimanite (Fig. 4c). Plagioclase commonly occurs at the contact of garnet porphyroblasts and matrix biotite (Fig. 4e). Important textural features in the leucocratic bands include the presence of perthite and antiperthite with sillimanite- and biotite-bearing inclusion trails (S_i; Fig. 4f). Plagioclase at the interstices of coarse quartz grains is interpreted to be crystallized melt films (Fig. 4g). Extensive recrystallization of coarse quartz and feldspar grains is noted in the leucocratic bands (Fig. 4h).

The presence of biotite, sillimanite and quartz inclusions in garnet porphyroblasts, and antiperthites in the leucosomes point to the following partial melting reaction during peak metamorphism:

$$\text{biotite} + \text{sillimanite} + \text{plagioclase} + \text{quartz} \rightarrow \text{garnet} + \text{K} - \text{feldspar} + \text{melt} \qquad (2)$$

The formation of biotite- and sillimanite-bearing symplectites replacing K-feldspar (yellow arrows, Fig. 4c) and biotite replacing garnet along fractures (blue arrows, Fig. 4c) indicate retrogression. Symplectites of biotite + sillimanite also occur at the contact of peritectic garnet and the leucocratic layers (yellow arrows, Fig. 4c).

Garnet porphyroblasts in the mesocratic layers are mostly solid solutions of pyrope and almandine with negligible spessartine and very low grossular contents (Table 1b; analytical methods are given in the Appendix). Garnet porphyroblasts show no or only very weak compositional variation from cores ($Prp_{0.20–0.22}$ $Alm_{0.73–0.75}$ $Sps_{0.01}Grs_{0.04–0.05}$ and X_{Mg} ~0.21–0.23) to outer rims ($Prp_{0.22}Alm_{0.73}Sps_{0.01}Grs_{0.04}$ and X_{Mg} ~0.23; Table 1b). At the contacts with biotite inclusions and at the edges against matrix biotite grains, garnet compositions show a decrease in pyrope contents ($Prp_{0.16–0.19}$ $Alm_{0.75–0.79}$ $Sps_{0.01}Grs_{0.04–0.05}$ and X_{Mg} ~0.17–0.20; Table 1b). Titanium contents of biotite inclusions in garnet porphyroblasts vary from 0.189–0.223 apfu and their X_{Mg} values range from 0.66–0.69 (Table 1b). Titanium contents of cores and rims of matrix biotite grains at contacts with garnet rims vary from 0.211–0.239 and 0.202–0.231 apfu, respectively (Table 1b). X_{Mg} of the cores and rims of matrix biotite grains at contacts with garnet grains vary from 0.59–0.61 and 0.61–0.65, respectively (Table 1b). X_{An} of plagioclase grains within the leucocratic layers (0.33–0.37) are higher than those of the plagioclase which occurs in the garnet fractures (0.25–0.27; Table 1b).

feldspar-bearing leucocratic bands (c). Inclusion trails in garnet porphyroblasts (S_i) are formed by biotite + sillimanite + quartz; biotite fills up fractures in garnet (blue arrows); biotite + sillimanite-bearing symplectites replace potash feldspar in leucocratic bands and also occur at the margins of garnet porphyroblasts against the leucocratic bands (yellow arrows). (e) BSE image of BJ-30 showing occurrence of plagioclase at margins of garnet. (f–h) Thin-section images of leucocratic bands of BJ-30 showing perthite, antiperthite texture and recrystallization of quartz and feldspar grains. Note presence of inclusion trails (S_i) of biotite + sillimanite in an antiperthite grain.

Table 1a. Representative mineral chemical analyses of garnet from BJ-28

	Profile-1				Profile-2									
Texture	C	IR	OR	E^Bt (M)	C	IR	IR	E^Qtz (M)	E^Bt (M)	C^Bt (I)	C^Bt (I)	C^Bt (I)	C^Bt (I)	E^Bt (M)
SiO_2	37.12	37.15	37.26	37.40	37.2	37.17	37.31	36.81	36.73	37.21	36.93	36.91	37.16	37.05
TiO_2	0.00	0.00	0.00	0.00	0.04	0.01	0.01	0.00	0.00	0.00	0.03	0.00	0.00	0.00
Al_2O_3	20.78	20.86	20.71	20.87	20.83	20.73	20.78	20.73	20.49	20.66	20.54	20.73	20.68	20.84
Cr_2O_3	0.01	0.06	0.00	0.01	0.00	0.01	0.02	0.00	0.00	0.03	0.03	0.00	0.00	0.00
FeO	36.18	36.16	35.99	37.30	36.71	36.28	36.70	36.71	37.72	36.33	36.74	36.82	36.75	37.88
MnO	1.99	1.90	1.99	1.91	2.03	1.99	1.97	2.04	2.08	1.95	1.81	2.04	1.99	2.04
MgO	2.64	2.72	2.61	2	2.75	2.62	2.61	2.44	1.98	2.38	2.27	2.3	2.33	1.84
CaO	1.35	1.28	1.24	0.96	1.24	1.26	1.21	1.22	0.97	1.17	1.19	1.16	1.14	1.25
Na_2O	0.01	0.01	0.03	0.00	0.00	0.03	0.01	0.00	0.01	0.00	0.01	0.01	0.01	0.00
K_2O	0.00	0.01	0.00	0.00	0.00	0.01	0.00	0.02	0.00	0.00	0.02	0.00	0.00	0.00
Totals	100.11	100.18	99.83	100.45	100.88	100.14	100.65	100.04	100.05	99.73	99.57	100	100.07	100.96
Oxygens	12	12	12	12	12	12	12	12	12	12	12	12	12	12
Si	3.000	2.999	3.018	3.021	2.987	3.004	3.003	2.986	2.992	3.020	3.010	2.996	3.012	2.991
Ti	0.000	0.000	0.000	0.000	0.002	0.001	0.000	0.000	0.000	0.000	0.002	0.000	0.000	0.000
Al	1.980	1.986	1.977	1.987	1.972	1.975	1.972	1.982	1.968	1.977	1.973	1.984	1.977	1.983
Cr	0.001	0.004	0.000	0.001	0.000	0.001	0.001	0.000	0.000	0.002	0.002	0.000	0.000	0.000
Fe^{3+}	0.02	0.016	0.000	0.000	0.049	0.019	0.022	0.049	0.049	0.000	0.004	0.025	0.001	0.035
Fe^{2+}	2.426	2.426	2.437	2.520	2.416	2.434	2.448	2.441	2.521	2.466	2.500	2.475	2.491	2.522
Mn	0.136	0.130	0.137	0.131	0.138	0.136	0.134	0.140	0.144	0.134	0.125	0.140	0.137	0.140
Mg	0.318	0.327	0.315	0.241	0.329	0.315	0.313	0.295	0.241	0.288	0.276	0.278	0.281	0.221
Ca	0.117	0.110	0.108	0.083	0.107	0.109	0.104	0.106	0.085	0.102	0.104	0.101	0.099	0.108
Na	0.002	0.002	0.005	0.000	0.000	0.005	0.002	0.000	0.001	0.000	0.001	0.001	0.002	0.000
K	0.000	0.001	0.000	0.000	0.000	0.001	0.000	0.002	0.000	0.000	0.002	0.000	0.000	0.000
Sum	8	8	7.996	7.985	8	8	8	8	8	7.99	8	8	8	8
X_{Prp}	0.11	0.11	0.11	0.08	0.11	0.11	0.10	0.10	0.08	0.10	0.09	0.09	0.09	0.07
X_{Alm}	0.81	0.81	0.81	0.85	0.81	0.81	0.82	0.82	0.84	0.82	0.83	0.83	0.83	0.84
X_{Grs}	0.04	0.04	0.04	0.03	0.03	0.04	0.03	0.03	0.03	0.03	0.03	0.03	0.03	0.04
X_{Sps}	0.05	0.04	0.05	0.04	0.05	0.05	0.04	0.05	0.05	0.04	0.04	0.05	0.05	0.05
X_{Mg}	0.12	0.12	0.11	0.09	0.12	0.11	0.11	0.11	0.09	0.10	0.10	0.10	0.10	0.08

I – inclusion; M – matrix; C – core; R – rim; IR – inner rim; OR – outer rim; E – edge; Fr – fracture; F – foliation; ^ – against;
$X_{Mg} = Mg/(Mg + Fe^{2+})$;
$X_{Sps} = Mn/(Mn + Ca + Fe^{2+} + Mg)$; $X_{Alm} = Fe^{2+}/(Fe^{2+} + Mg + Ca + Mn)$; $X_{Prp} = Mg/(Fe^{2+} + Ca + Mn + Mg)$;
$X_{Grs} = (Al/(Fe^{3+} + Ti + Al + Cr))^{*}(Ca/(Fe^{2+} + Mg + Ca + Mn))$.

Table 1a. (Continued) Representative mineral chemical analyses of biotite from BJ-28

	Grain-1			Grain-2		Grain-3		Grain-4						
Texture	C	M (R^Grt)	M (R^Ms-Qtz)	M (C)	M (R^Grt)	M (C)	M (R^Grt)	M (C)	M (R^Grt)	I^Grt (C)	M (R^Grt)	I^Grt (C)	I^Grt (C)	I^Grt (C)
SiO_2	34.50	34.09	34.65	34.78	34.48	34.61	33.8	34.62	35.33	35.96	35.07	35.53	34.95	35.30
TiO_2	2.96	3.05	2.92	2.67	2.48	2.88	2.51	2.47	2.80	2.58	2.47	2.34	2.67	2.48
Al_2O_3	18.26	18.00	18.42	18.71	19.17	18.2	18.15	18.89	19.05	18.57	19.56	18.3	18.29	18.25
Cr_2O_3	0.00	0.04	0.02	0.00	0.00	0.00	0.00	0.02	0.03	0.00	0.01	0.06	0.04	0.00
FeO	22.64	23.12	23.28	22.41	21.65	22.65	22.94	21.59	22.13	20.10	21.27	19.88	20.04	20.41
MnO	0.03	0.03	0.04	0.02	0.05	0.00	0.00	0.03	0.04	0.00	0.05	0.05	0.00	0.05
MgO	6.5	6.56	6.82	6.85	6.78	6.71	6.88	7.07	6.96	9.52	7.00	9.08	8.63	8.72
CaO	0.00	0.00	0.00	0.00	0.00	0.00	0.00	0.00	0.00	0.05	0.00	0.05	0.02	0.03
Na_2O	0.15	0.12	0.12	0.17	0.15	0.14	0.10	0.18	0.12	0.18	0.19	0.16	0.17	0.17
K_2O	8.97	8.92	8.42	8.93	8.92	9.01	8.68	9.07	9.01	8.63	8.97	9.03	8.83	8.81
Totals	94.00	93.93	94.69	94.54	93.68	94.20	93.06	93.93	95.48	95.58	94.57	94.48	93.64	94.22
Oxygens	11	11	11	11	11	11	11	11	11	11	11	11	11	11
Si	2.706	2.686	2.695	2.704	2.696	2.709	2.684	2.702	2.711	2.721	2.705	2.729	2.712	2.724
Ti	0.174	0.181	0.171	0.156	0.146	0.169	0.150	0.145	0.161	0.147	0.143	0.135	0.156	0.144
Al	1.689	1.672	1.689	1.715	1.767	1.679	1.699	1.738	1.723	1.656	1.778	1.658	1.674	1.661
Cr	0.000	0.003	0.001	0.000	0.000	0.000	0.000	0.001	0.002	0.000	0.001	0.004	0.003	0.000
Fe^{3+}	0	0	0	0	0	0	0	0	0	0	0	0	0	0
Fe^{2+}	1.485	1.524	1.514	1.457	1.416	1.483	1.523	1.409	1.42	1.272	1.372	1.277	1.301	1.317
Mn	0.002	0.002	0.002	0.001	0.003	0.000	0.000	0.002	0.003	0.000	0.003	0.003	0.000	0.004
Mg	0.759	0.771	0.790	0.794	0.790	0.782	0.814	0.822	0.796	1.074	0.804	1.040	0.998	1.003
Ca	0.000	0.000	0.000	0.000	0.000	0.000	0.000	0.000	0.000	0.004	0.000	0.004	0.002	0.002
Na	0.023	0.019	0.018	0.026	0.022	0.021	0.016	0.027	0.018	0.027	0.028	0.024	0.025	0.025
K	0.897	0.896	0.836	0.886	0.890	0.900	0.879	0.903	0.882	0.833	0.882	0.885	0.874	0.867
Sum	7.736	7.754	7.717	7.739	7.731	7.743	7.765	7.749	7.716	7.735	7.718	7.759	7.744	7.748
X_{Mg}	0.34	0.34	0.34	0.35	0.36	0.35	0.35	0.37	0.36	0.46	0.37	0.45	0.43	0.43

Table 1a. (Continued) Representative mineral chemical analyses of muscovite from BJ-28

	M(F)	M(F)	M (R^Grt)	M (R^Grt)	M (R^Grt)	M (R^Grt)
SiO_2	48.88	47.29	48.47	48.55	49.42	47.52
TiO_2	0.44	0.59	0.54	0.41	0.49	0.46
Al_2O_3	36.43	34.33	35.97	36.23	36.69	36.00
Cr_2O_3	0.02	0.06	0.00	0.00	0.00	0.03
FeO	1.22	3.04	1.27	1.38	1.36	1.49
MnO	0.00	0.00	0.00	0.01	0.02	0.03
MgO	0.60	1.31	0.56	0.60	0.59	0.60
CaO	0.00	0.00	0.00	0.00	0.00	0.00
Na_2O	0.58	0.50	0.66	0.60	0.61	0.55
K_2O	10.52	10.26	10.23	10.17	10.20	10.30
Totals	98.69	97.62	97.71	97.94	99.37	96.99
Oxygens	11	11	11	11	11	11
Si	3.125	3.085	3.129	3.125	3.132	3.098
Ti	0.021	0.029	0.026	0.020	0.023	0.023
Al	2.746	2.640	2.737	2.749	2.741	2.768
Cr	0.001	0.003	0.000	0.000	0.000	0.001
Fe^{3+}	0.000	0.112	0.000	0.000	0.000	0.000
Fe^{2+}	0.065	0.054	0.069	0.074	0.072	0.081
Mn	0.000	0.000	0.000	0.000	0.001	0.002
Mg	0.057	0.127	0.054	0.058	0.055	0.058
Ca	0.000	0.000	0.000	0.000	0.000	0.000
Na	0.072	0.063	0.082	0.075	0.075	0.069
K	0.858	0.854	0.842	0.835	0.825	0.857
Sum	6.946	6.968	6.940	6.936	6.925	6.958

Table 1b. Representative mineral chemical analyses of garnet from BJ-30

											Profile-1			
Texture	OR	C^Fr	C^Bt (I)	C^Bt (I)	E^Bt (M)	E^Bt (M)	E^Bt (M)	OR^Bt (I)	E^Bt-Pl	E^Bt-Pl	C^Sil (I)	OR	IR	E^Bt (M)
SiO_2	37.94	37.79	38.09	38.19	37.70	37.79	37.50	37.97	37.47	37.53	37.74	37.71	37.90	37.65
TiO_2	0.05	0.02	0.00	0.05	0.00	0.05	0.00	0.00	0.00	0.00	0.00	0.00	0.00	0.00
Al_2O_3	21.29	21.13	21.23	21.27	21.18	21.06	20.88	21.25	20.88	21.14	20.95	21.12	21.2	21.13
Cr_2O_3	0.02	0.00	0.00	0.00	0.02	0.00	0.02	0.07	0.00	0.06	0.10	0.03	0.00	0.00
FeO	33.25	33.61	33.92	33.40	35.48	35.32	34.46	34.19	34.43	34.67	33.77	33.56	32.89	34.20
MnO	0.27	0.32	0.31	0.31	0.33	0.41	0.32	0.33	0.41	0.36	0.35	0.39	0.31	0.32
MgO	5.65	5.26	5.08	5.38	3.97	3.93	4.41	4.81	4.52	4.45	5.09	5.55	5.44	4.79
CaO	1.46	1.47	1.61	1.58	1.58	1.61	1.67	1.66	1.57	1.53	1.52	1.39	1.46	1.72
Na_2O	0.01	0.00	0.00	0.01	0.01	0.03	0.01	0.03	0.01	0.02	0.00	0.00	0.00	0.00
K_2O	0.00	0.01	0.02	0.01	0.02	0.03	0.00	0.00	0.00	0.01	0.00	0.00	0.00	0.00
Totals	99.93	99.62	100.25	100.19	100.29	100.21	99.26	100.30	99.30	99.79	99.52	99.81	99.19	99.83
Oxygens	12	12	12	12	12	12	12	12	12	12	12	12	12	12
Si	3.002	3.007	3.014	3.016	3.007	3.015	3.012	3.009	3.008	2.999	3.011	2.993	3.017	3.000
Ti	0.003	0.001	0.000	0.003	0.000	0.003	0.000	0.000	0.000	0.000	0.000	0.000	0.000	0.000
Al	1.986	1.982	1.980	1.979	1.991	1.981	1.977	1.985	1.976	1.991	1.971	1.976	1.990	1.985
Cr	0.001	0.000	0.000	0.000	0.001	0.000	0.001	0.004	0.000	0.004	0.006	0.002	0.000	0.000
Fe^{3+}	0.005	0.002	0.000	0.000	0.000	0.000	0.000	0.000	0.010	0.011	0.001	0.036	0.000	0.016
Fe^{2+}	2.195	2.235	2.245	2.206	2.367	2.357	2.314	2.266	2.301	2.306	2.252	2.192	2.19	2.262
Mn	0.018	0.022	0.021	0.021	0.022	0.028	0.021	0.022	0.028	0.025	0.023	0.026	0.021	0.021
Mg	0.666	0.624	0.600	0.633	0.471	0.467	0.528	0.568	0.540	0.530	0.605	0.657	0.645	0.569
Ca	0.124	0.126	0.136	0.134	0.135	0.137	0.144	0.141	0.135	0.131	0.130	0.118	0.124	0.147
Na	0.001	0.000	0.000	0.001	0.001	0.005	0.001	0.004	0.002	0.002	0.000	0.000	0.000	0.000
K	0.000	0.001	0.002	0.001	0.002	0.003	0.000	0.000	0.000	0.001	0.000	0.000	0.000	0.000
Sum	8	8	7.997	7.993	7.998	7.995	7.999	7.999	8	8	8	8	7.988	8
X_{Prp}	0.22	0.21	0.20	0.21	0.16	0.16	0.18	0.19	0.18	0.18	0.20	0.22	0.22	0.19
X_{Alm}	0.73	0.74	0.75	0.74	0.79	0.79	0.77	0.76	0.77	0.77	0.75	0.73	0.73	0.75
X_{Sps}	0.01	0.01	0.01	0.01	0.01	0.01	0.01	0.01	0.01	0.01	0.01	0.01	0.01	0.01
X_{Grs}	0.04	0.04	0.05	0.04	0.05	0.05	0.05	0.05	0.04	0.04	0.04	0.04	0.04	0.05
X_{Mg}	0.23	0.22	0.21	0.22	0.17	0.17	0.19	0.20	0.19	0.19	0.21	0.23	0.23	0.20

I – inclusion; M – matrix; C – core; IR – inner rim; OR – outer rim; E – edge; Fr – fracture; ^ – against; $X_{Mg} = Mg/(Mg + Fe^{2+})$; $X_{Sps} = Mn/(Mn + Ca + Fe^{2+} + Mg)$; $X_{Alm} = Fe^{2+}/(Fe^{2+} + Mg + Ca + Mn)$; $X_{Prp} = Mg/(Fe^{2+} + Ca + Mn + Mg)$; $X_{Grs} = (Al/(Fe^{3+} + Ti + Al + Cr))*(Ca/(Fe^{2+} + Mg + Ca + Mn))$.

Table 1b. (Continued) Representative mineral chemical analyses of biotite from BJ-30

Texture	I^Grt (C)	I^Grt (C)	I^Grt (OR)	M (C)	M (C)	M (C)	M (C)	M (R)^Grt	M (R)^Grt	M (R)^Grt	M (R)^Grt	S^Kfs (L)
SiO_2	37.24	37.43	37.13	36.61	36.55	36.08	36.58	35.84	37.02	36.81	37.05	36.34
TiO_2	3.38	3.81	3.99	3.73	3.73	3.95	4.21	4.01	3.83	3.57	3.63	4.07
Al_2O_3	16.93	17.00	16.69	16.33	16.40	15.90	16.10	16.10	16.51	16.40	16.28	16.42
Cr_2O_3	0.05	0.01	0.04	0.00	0.00	0.06	0.00	0.03	0.00	0.05	0.01	0.02
FeO	12.61	11.76	12.82	14.89	14.77	15.06	14.99	14.35	13.39	14.97	14.90	15.52
MnO	0.00	0.00	0.00	0.00	0.01	0.02	0.00	0.00	0.00	0.00	0.00	0.01
MgO	14.17	14.64	14.11	13.05	12.83	12.36	12.64	12.73	14.03	12.97	13.18	11.97
CaO	0.01	0.00	0.00	0.00	0.00	0.00	0.00	0.02	0.00	0.04	0.03	0.02
Na_2O	0.18	0.21	0.21	0.13	0.11	0.12	0.15	0.18	0.16	0.13	0.09	0.10
K_2O	9.61	9.52	9.80	9.79	9.54	9.54	9.70	9.47	9.74	8.89	9.49	9.84
Totals	94.16	94.39	94.8	94.53	93.95	93.09	94.37	92.72	94.67	93.81	94.67	94.31
Oxygens	11	11	11	11	11	11	11	11	11	11	11	11
Si	2.777	2.77	2.759	2.759	2.765	2.765	2.762	2.749	2.762	2.779	2.779	2.755
Ti	0.189	0.212	0.223	0.211	0.212	0.228	0.239	0.231	0.215	0.202	0.205	0.232
Al	1.488	1.484	1.462	1.451	1.463	1.437	1.434	1.456	1.451	1.459	1.440	1.467
Cr	0.003	0.001	0.003	0.000	0.000	0.004	0.000	0.002	0.000	0.003	0.001	0.001
Fe^{3+}	0.000	0.000	0.000	0.000	0.000	0.000	0.000	0.000	0.000	0.000	0.000	0.000
Fe^{2+}	0.786	0.728	0.797	0.939	0.935	0.965	0.947	0.920	0.835	0.945	0.935	0.984
Mn	0.000	0.000	0.000	0.000	0.001	0.001	0.000	0.000	0.000	0.000	0.000	0.001
Mg	1.575	1.615	1.563	1.466	1.447	1.411	1.422	1.455	1.559	1.459	1.473	1.353
Ca	0.001	0.000	0.000	0.000	0.000	0.000	0.000	0.002	0.000	0.003	0.003	0.001
Na	0.025	0.030	0.031	0.019	0.016	0.018	0.022	0.027	0.023	0.018	0.014	0.015
K	0.915	0.899	0.929	0.941	0.921	0.933	0.934	0.926	0.927	0.856	0.908	0.952
Sum	7.759	7.741	7.766	7.785	7.761	7.763	7.761	7.768	7.773	7.725	7.758	7.762
X_{Mg}	0.67	0.69	0.66	0.61	0.61	0.59	0.60	0.61	0.65	0.61	0.61	0.58

I – inclusion; M – matrix; C – core; R – rim; OR – outer rim; L – leucosome; S – symplectite; ^ – against; $X_{Mg} = Mg/(Mg + Fe^{2+})$.

Table 1b. (Continued) Representative mineral chemical analyses of feldspar from BJ-30

Texture	Pl M (C) _L	Pl M (C) _L	Pl M (C) _L	Pl M (C) _L	Pl M (C) _L	Pl M (C) _L	Pl M (C) _L	Pl ^Grt (Fr)	Pl ^Grt (Fr)	Pl ^Grt (Fr)	Pl M^Grt (R)	Pl M^Grt (R)	Kfs M (C) _L	Kfs M (C) _L
SiO_2	58.52	58.26	58.66	59.02	58.82	58.5	59.09	60.86	61.07	61.37	60.93	61.05	64.54	64.72
TiO_2	0.00	0.03	0.00	0.00	0.00	0.01	0.02	0.00	0.04	0.00	0.00	0.00	0.02	0.00
Al_2O_3	25.99	25.94	25.89	25.89	25.60	25.82	25.41	24.28	24.24	24.02	23.89	24.15	18.30	18.43
Cr_2O_3	0.00	0.00	0.00	0.00	0.00	0.01	0.04	0.00	0.00	0.00	0.03	0.00	0.00	0.00
FeO	0.04	0.00	0.02	0.00	0.02	0.01	0.02	0.30	0.28	0.30	0.42	0.53	0.00	0.01
MnO	0.00	0.02	0.00	0.00	0.00	0.00	0.00	0.00	0.00	0.00	0.00	0.00	0.00	0.03
MgO	0.00	0.00	0.00	0.01	0.00	0.00	0.00	0.00	0.02	0.01	0.00	0.02	0.00	0.00
CaO	7.97	8.16	7.76	7.81	7.69	7.95	7.29	6.07	6.09	5.59	5.69	5.76	0.00	0.00
Na_2O	7.51	7.49	7.73	7.66	7.89	7.59	8.03	8.82	9.01	9.15	9.04	8.95	1.18	1.75
K_2O	0.14	0.23	0.23	0.16	0.16	0.17	0.14	0.05	0.06	0.06	0.07	0.07	15.01	14.38
Totals	100.17	100.11	100.30	100.55	100.19	100.06	100.05	100.41	100.84	100.53	100.11	100.59	99.04	99.32
Oxygens	8	8	8	8	8	8	8	8	8	8	8	8	8	8
Si	2.616	2.610	2.620	2.627	2.630	2.619	2.642	2.703	2.703	2.720	2.714	2.707	2.999	2.994
Ti	0.000	0.001	0.000	0.000	0.000	0.000	0.001	0.000	0.001	0.000	0.000	0.000	0.001	0.000
Al	1.370	1.370	1.364	1.358	1.349	1.363	1.340	1.271	1.265	1.255	1.255	1.263	1.002	1.005
Cr	0.000	0.000	0.000	0.000	0.000	0.000	0.001	0.000	0.000	0.000	0.001	0.000	0.000	0.000
Fe^{3+}	0.001	0.000	0.001	0.000	0.001	0.000	0.001	0.011	0.010	0.011	0.016	0.020	0.000	0.000
Fe^{2+}	0.000	0.000	0.000	0.000	0.000	0.000	0.000	0.000	0.000	0.000	0.000	0.000	0.000	0.000
Mn	0.000	0.001	0.000	0.000	0.000	0.000	0.000	0.000	0.000	0.000	0.000	0.000	0.000	0.001
Mg	0.000	0.000	0.000	0.000	0.000	0.000	0.000	0.000	0.001	0.001	0.000	0.001	0.000	0.000
Ca	0.382	0.391	0.372	0.372	0.368	0.381	0.349	0.289	0.289	0.265	0.272	0.274	0.000	0.000
Na	0.651	0.650	0.670	0.661	0.684	0.659	0.696	0.759	0.773	0.786	0.781	0.770	0.106	0.157
K	0.008	0.013	0.013	0.009	0.009	0.009	0.008	0.003	0.004	0.003	0.004	0.004	0.890	0.849
Sum	5.028	5.036	5.039	5.029	5.042	5.033	5.038	5.036	5.046	5.042	5.042	5.038	4.998	5.007
X_{An}	0.37	0.37	0.35	0.36	0.35	0.36	0.33	0.27	0.27	0.25	0.26	0.26		

I – inclusion; M – matrix; C – core; R – rim; Fr – fracture; ^ – against; _ – within; L – leucosome; $X_{An} = Ca/(Ca + Na + K)$.

3.b. *P–T* conditions of anatexis

3.b.1. Thermodynamic modelling

Microtextures and mineral assemblages of the investigated gneisses (BJ-28 and BJ-30) of the Aravalli Supergroup rocks (shown in Fig. 4a–h) point to muscovite and/or biotite breakdown reactions during extensive anatexis and garnet formation. The investigated rocks show migmatitic textures where melt migrated from the reaction sites and segregated as distinct domains and layers resulting in complete recrystallization and obliteration of the palaeosomes (Fig. 3a–c).

This imparts difficulty in estimation of the palaeosome bulk composition for pseudosection analysis. In order to address this problem, in previous petrological studies of migmatites, two different methods have been adopted for constraining the bulk composition for pseudosection analyses. In one method, pseudosections have been constructed with various hypothetical bulk compositions of the pelites (White, Powell & Holland, 2001, 2007; Johnson & Brown, 2004), and in the second method, bulk compositions were reconstituted from mineral modes and compositions from different microdomains (Kelsey *et al.* 2003). Melt reintegration is problematic for the migmatite samples BJ-28 and BJ-30 owing to strong deformation and the cumulate origin of some of the leucocratic layers or domains (e.g. Johnson & Brown, 2004). So we have considered modelling of the melting reactions by constructing *P*–*T* pseudosections using the average hypothetical pelite bulk composition of White, Powell & Holland (2001) in the model system Na_2O–CaO–K_2O–FeO–MgO–Al_2O_3–SiO_2–H_2O (NCKFMASH) in order to estimate the (i) temperature of melting, and (ii) *P*–*T* ranges of stability of the assemblages formed during peak or near-peak metamorphism for each rock. Additionally, in order to estimate *P*–*T* conditions of equilibration of restite phases during peak and post-peak metamorphic conditions, *P*–*T* pseudosections have been constructed from the refractory bulk compositions (determined by XRF) of the mesocratic bands of BJ-28 and BJ-30. Analytical conditions of XRF analysis are given in the Appendix.

Pseudosections have been constructed using PERPLE_X (Connolly, 2005) and the thermodynamic database of Holland & Powell (1998), modified in 2004. Solution models of phases used for pseudosection modelling are: (i) garnet: hybrid model of Holland & Powell (1998) and Engi & Wersin (1987); (ii) biotite: White, Powell & Holland (2007); (iii) muscovite: hybrid model of Coggon & Holland (2002) and Auzanneau *et al.* (2010); (iv) feldspar: Benisek, Dachs & Kroll (2010), Newton, Charlu & Kleppa (1980) and Waldbaum & Thompson (1968); (v) melt: hybrid model of Holland & Powell (2001) and White, Powell & Holland (2001).

3.b.2. *Results of P–T pseudosection analyses*

At first, *P*–*T* pseudosections were constructed using the hypothetical metapelite bulk composition of White, Powell & Holland (2001). Both the ternary feldspar model of Benisek, Dachs & Kroll (2010) and plagioclase model of Newton, Charlu & Kleppa (1980), and K-feldspar model of Waldbaum & Thompson (1968) were used to model formation of perthite and/or antiperthite and the occurrence of plagioclase and K-feldspar as separate phases either in the mesocratic or in the leucocratic layers of BJ-28 and BJ-30 (Fig. 5a–d). In the *P*–*T* pseudosections in Figure 5a, b the melt-in curve has positive slopes with slopes becoming very steep at >8 kbar. At the pressure range of 4–12 kbar, which has been chosen for the *P*–*T* pseudosections, the partial melting reaction initiates by muscovite breakdown at lower temperatures and by biotite breakdown at higher temperatures (Fig. 5a–d).

The aluminosilicate-absent biotite + muscovite + garnet + quartz + feldspar + melt-bearing assemblage in BJ-28 formed during peak metamorphism is stable at pressures >10 kbar (Fig. 5a, c). X_{Mg} isopleths of garnet (0.08–0.14) and biotite inclusions in garnet (0.46) corresponding to the values measured in BJ-28 intersect at temperatures of ~725 °C and at lower pressures (~7.5 kbar) in the fields where sillimanite is stable with biotite + melt (~12 modal %) + feldspar(s) + muscovite + garnet + quartz (Fig. 5b, d). Such a disparity in mineral assemblage may be attributed to some difference in hypothetical bulk composition and the real palaeosome bulk composition. Maximum melt abundance at the temperature calculated from the isopleth thermobarometry of garnet and biotite is ~20 mol. % (Fig. 5a, c).

The peak assemblage of BJ-30 is biotite + garnet + sillimanite + plagioclase + K- feldspar + melt + quartz (Fig. 4c). This assemblage is stable in the *P*–*T* range of 4–9 kbar and 740–825 °C, in the *P*–*T* pseudosection constructed from the hypothetical bulk composition of White, Powell & Holland (2001; Fig. 5a, c). X_{Mg} isopleths of garnet and biotite corresponding to the measured compositions (garnet ~0.21 and biotite ~0.6–0.7; Table 1b) plot at ~780–800 °C along the biotite-out curve within the garnet + biotite + melt + feldspar + quartz-bearing field and possibly indicate near-peak temperature (T_{Max}; Fig. 5b, d). Maximum pressure in BJ-30 during peak metamorphism is estimated from the intersections of the compositional isopleths with the sillimanite to kyanite transition curve, i.e. at ~8 kbar (Fig. 5b, d). This pressure is similar to that noted for the Palaeoproterozoic sillimanite-facies partial melting event recorded from the SC by Saha *et al.* (2008). The computed melt volume at the estimated peak conditions (P_{Max}= 8 kbar and T_{Max}=780–800 °C) is ~42 % (Fig. 4a, b).

As the second approach, *P*–*T* pseudosections were constructed from the bulk composition of the mesocratic domains of the rock which represent the refractory bulk compositions after extensive melt segregation. The bulk rock compositions determined by X-ray fluorescence analysis are given in Table 2. The refractory bulk composition of the muscovite-bearing BJ-28 has higher X_{Mg} (0.43) than that of the biotite-bearing BJ-30 (0.20) and of the average hypothetical bulk composition of the pelitic rocks (0.26). Al_2O_3 and K_2O contents of the hypothetical bulk composition are higher than that of BJ-28, BJ-30 and the hypothetical bulk composition (Appendix Table A1). On the contrary its CaO content is lower than that of BJ-28 and BJ-30 (Appendix Table A1).

Pseudosections constructed from the XRF bulk composition of the mesocratic band of BJ-28 (in the NCKFMASH system using the identical water content to that of White, Powell & Holland 2001) is shown

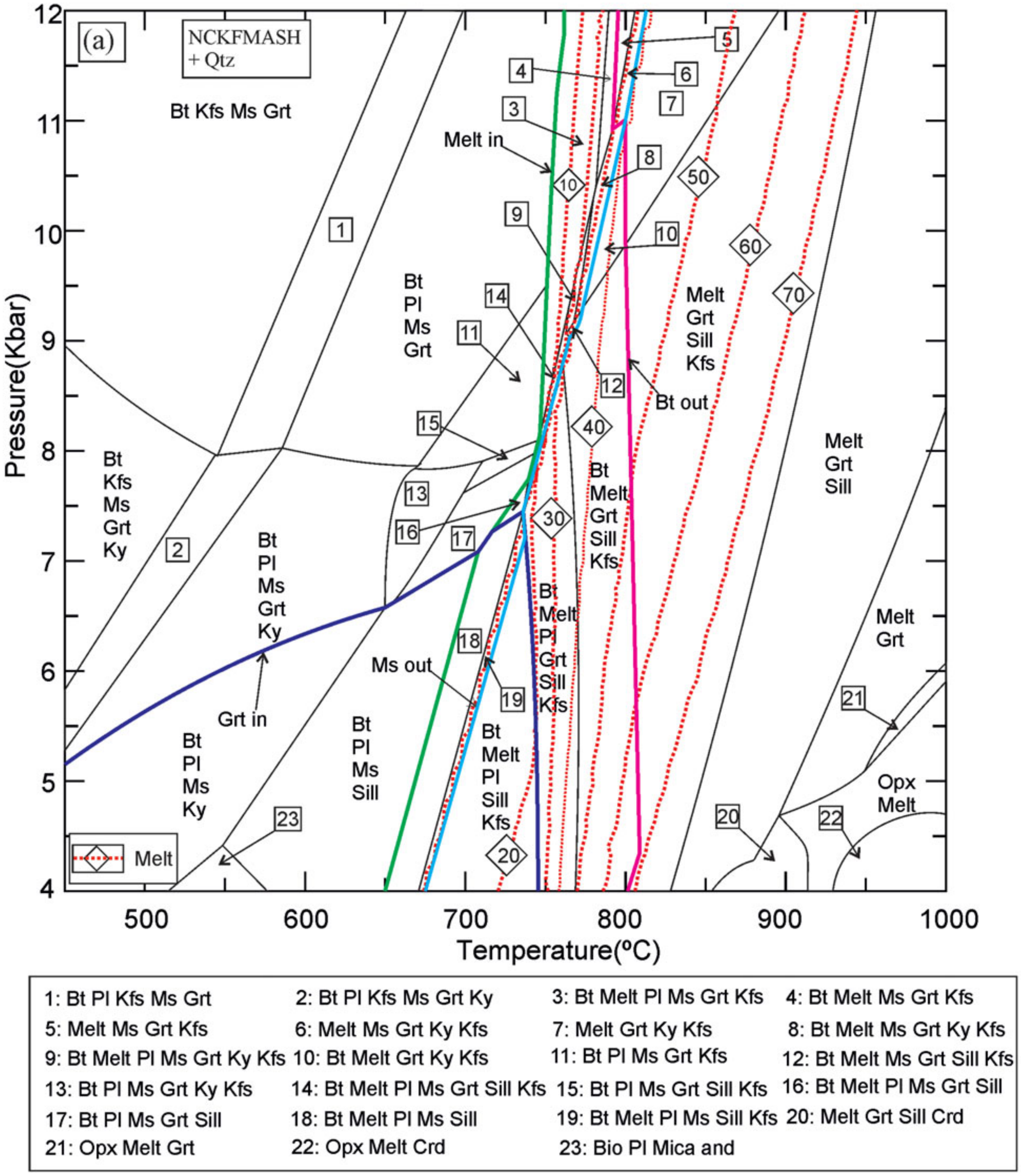

Figure 5. (Colour online) (a) *P–T* pseudosection for the average pelite composition used in White, Powell & Holland (2001). The bulk composition in mol. % is $Al_2O_3 = 30.66$, $FeO = 23.74$, $MgO = 12.47$, $CaO = 0.97$, $Na_2O = 1.94$, $K_2O = 9.83$ and $H_2O = 20.39$; SiO_2 has been taken as a saturated component. The ternary feldspar solution model of Benisek, Dachs & Kroll (2010) has been used for this *P–T* pseudosection. Abundances of melt are shown as isopleths.

in Figure 6a, b. *P–T* pseudosections demonstrate that melting reactions occur from 650 °C at 4 kbar to *c.* 600 °C at 12 kbar, i.e. within a very narrow temperature range, and at >600–650 °C vapour-absent melting is prevalent (Fig. 6a). The peak assemblage of biotite + garnet + quartz + melt is stable between 7–12 kbar and 600–800 °C (Fig. 6a). Garnet X_{Mg} isopleths corresponding to those measured from a garnet porphyroblast (both core and rims) plot along the 650–700 °C range (Fig. 6b). X_{Mg} isopleths similar to the measured composition of the biotite inclusions (~0.43–0.46; Table 1a) in the garnet core also plot in the same temperature range. However, the isopleths corresponding to the composition of the matrix biotite (~0.34) do not match this stability field (Fig. 6b). Si isopleths for muscovite values (~3.09), similar to the measured composition, intersect with isopleths of garnet and biotite at ~8 kbar and 700 °C (Fig. 6b).

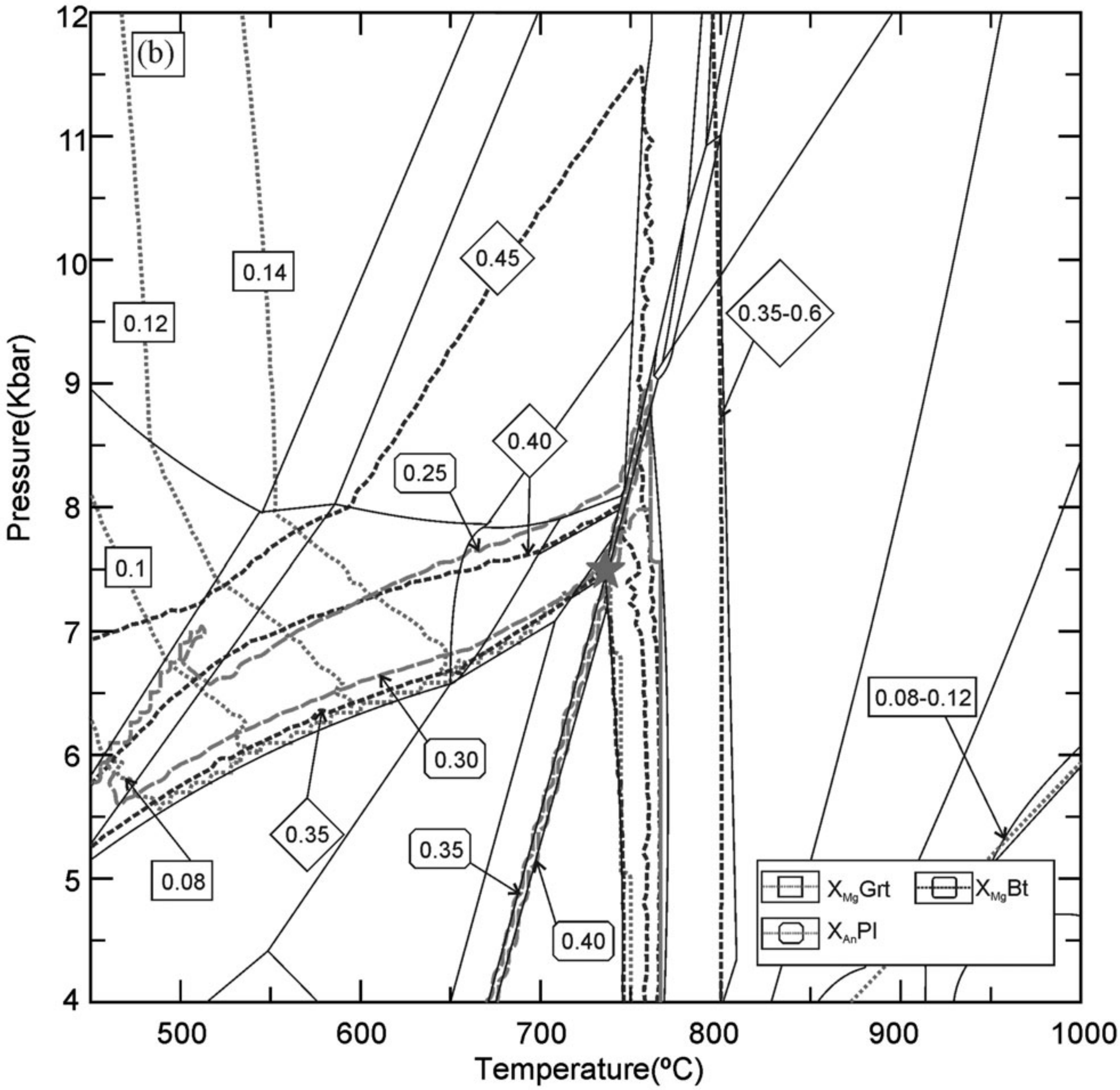

Figure 5. (Continued) (Colour online) (b) Compositional isopleths of garnet and biotite in the *P*–*T* pseudosection of (a).

Table 2. X-ray fluorescence analyses of sample in weight per cent

Sample	BJ-28	BJ-30
SiO_2	61.59	47.40
TiO_2	0.77	1.67
Al_2O_3	16.74	19.63
Fe_2O_3	8.48	25.18
MnO	0.07	0.27
MgO	2.94	3.11
CaO	1.74	1.24
K_2O	3.11	1.10
Na_2O	3.36	0.22
P_2O_5	0.06	0.50
SUM	98.86	100.32
LOI	0.96	0.50

The calculated abundance of melt at ~650–700 °C is ~30 % (Fig. 6a). Melt volume percentages at the peak *P*–*T* conditions are ~30–31 % (Fig. 6a), which is much higher than the melt escape threshold value of ~20 vol. % estimated by Vigneresse, Barbey & Cuney (1996). As the bulk composition used for the pseudosection analyses is refractory, it may be predicted that the protolith (expected to be more fertile) would have yielded higher volumes (>30 %) of melt leading to complete migration and segregation of the melt as has been observed in the outcrop (Fig. 3b).

The *P*–*T* pseudosection for BJ-30 from the bulk composition derived by XRF analysis (Table 2) and calculated in the (Na_2O–CaO–K_2O–FeO–MgO–Al_2O_3–SiO_2–H_2O–TiO_2) NCKFMASHTi system (Fig. 7a, b), depicts *P*–*T* conditions for water-saturated partial melting. The peak metamorphic assemblage garnet + biotite ± plagioclase + melt + sillimanite + quartz + ilmenite according to the pseudosection (Fig. 7a) is stable at 4–7 kbar and 725–780 °C. Isopleths of garnet X_{Mg} corresponding to the

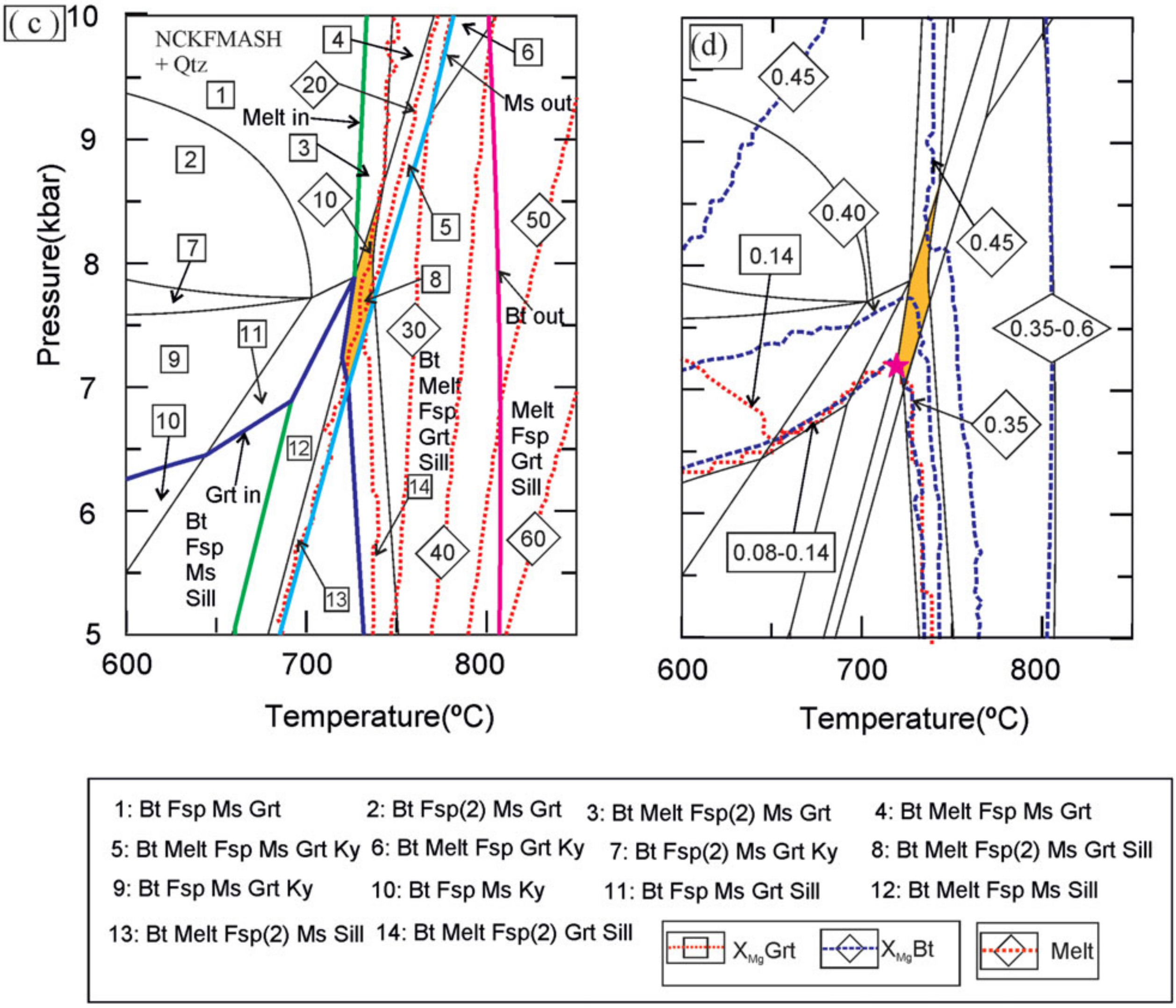

Figure 5. (Continued) (Colour online) (c) *P–T* pseudosection for the average pelite composition used in White, Powell & Holland (2001) with feldspar model of Newton, Charlu & Kleppa (1980) and Waldbaum & Thompson (1968) to model occurrence of plagioclase and potash feldspar as separate phases. (d) Compositional isopleths of garnet, biotite and feldspar in the *P–T* pseudosection of (c).

measured values (~0.20; Table 1b) plot at ~755 °C (Fig. 7b).

3.b.3. Conventional geothermometry

Garnet–biotite thermometry has been conducted from the samples BJ-30 and BJ-28, in order to estimate temperatures of garnet formation during partial melting and post-peak re-equilibration. The thermometry has been applied at a ~8 kbar reference pressure, estimated from the pseudosection analysis. Additionally, the titanium-in-biotite geothermometer of Henry, Guidotti & Thomson (2005) was also applied to determine temperatures of partial melting and cooling.

Garnet–biotite thermometry from the garnet cores and biotite inclusions in BJ-28 yields temperatures of ~500–516 °C and from the garnet edges against matrix biotite rims ~507–560 °C (Table 3a). Temperatures obtained from titanium contents in biotite inclusions in garnet porphyroblasts range between ~638 and 659 °C and those from matrix biotite grains between 638 and 672 °C (Table 3b). Although the highest temperature obtained from titanium-in-biotite thermometry (~672 °C) is close to the temperatures of muscovite melting and garnet formation at ~710 °C obtained from pseudosection analyses (Fig. 6a, b), temperatures obtained from garnet–biotite thermometry are significantly lower (more than ~100 °C), which is interpreted as a result of strong diffusion rates of Fe and Mg at supra-solidus conditions.

For sample BJ-30, temperatures obtained from garnet–biotite thermometry from the garnet core compositions and biotite inclusions of ~500–509 °C are similar to those obtained from the compositions of garnet edges and matrix biotite rims (~500–515 °C; Table 1a). Titanium-in-biotite thermometry conducted from biotite inclusions in garnet yields temperatures ranging from 743–765 °C and from the matrix biotite grains yields temperatures of ~741–754 °C

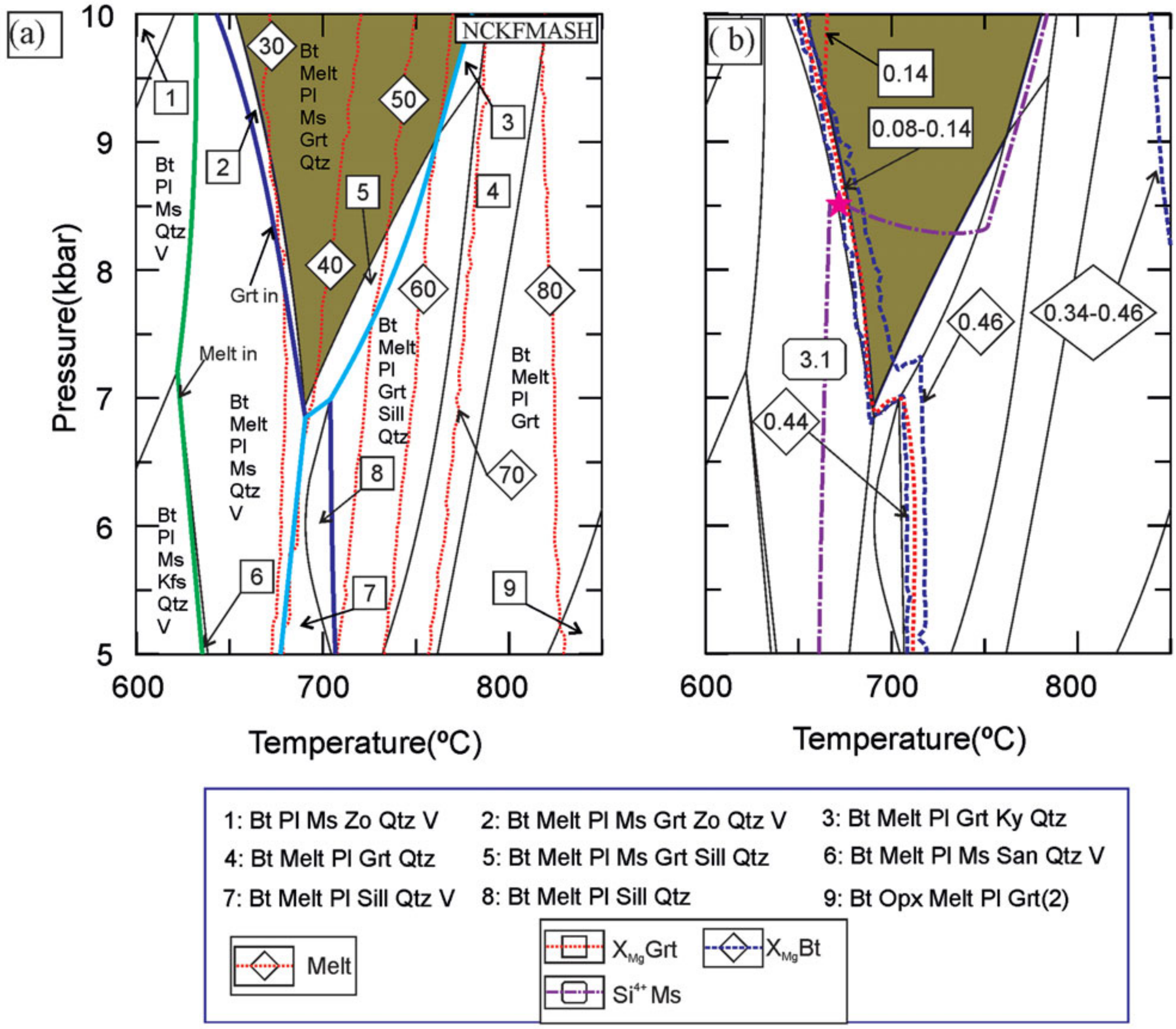

Figure 6. (Colour online) (a) *P–T* pseudosections in NCKFMASH system from bulk composition of mesocratic band of BJ-28. The bulk composition in mol. % is $SiO_2 = 69.43$, $Al_2O_3 = 11.12$, $FeO = 6.53$, $MgO = 5.00$, $CaO = 2.087$, $Na_2O = 2.42$, $K_2O = 3.39$ and $H_2O = 20.39$. Isopleths show melt abundance. (b) Compositional isopleths of garnet and biotite in the *P–T* pseudosection of (a).

(Table 1b). A temperature range of ~740–765 °C obtained from titanium contents in biotite grains is close to ~780 °C, obtained from garnet isopleth thermometry in the pseudosection (Fig. 7a, b). On the contrary, garnet–biotite thermometry yields the minimum blocking temperature between garnet and biotite at ~500 °C similar to that obtained in BJ-28.

4. Monazite dating

Both studied metapelite samples are rich in monazite. In sample BJ-28, monazite is found only in the matrix either enclosed by biotite, muscovite (Fig. 8d) and quartz, or intergrown with apatite. Monazite from sample BJ-30 also most commonly occurs in the fine-grained, quartz–biotite, quartz–K-feldspar or sillimanite matrix (Fig. 8g), but some grains (mnz7, 11–14) occur enclosed by garnet (Fig. 8h). Monazite crystals are mostly anhedral to subhedral, typically 40–100 µm (BJ-28) or 80–130 µm in size (BJ-30). Back-scattered electron (BSE) images from both samples show that they are either homogeneous or may contain a darker (Y-enriched) phase in the centres (Fig. 8a, b, g). Several larger grains from BJ-28 show a more complicated structure with bright patches enriched in Th.

Monazites were dated by electron microprobe Cameca SX-100 in Bratislava using the ‘age calibration’ approach (Petrík & Konečný, 2009), which includes spot analyses yielding apparent ages. These are then corrected against five age standards dated isotopically by SHRIMP and TIMS methods. Analytical settings were set as follows: counting times for Pb 150 s, Th 45 s, U 75 s, Y 45 s, and for all other elements 25–35 s; sample current 100–130 nA; beam diameter as large as possible, up to 10 µm, but mostly 3 µm to get maximum counts and to minimize surface damage. Standards used were: rare earth elements (REEs) and Y from phosphates XPO_4, Th from ThO_2, Pb from galena, U from UO_2, Ca and Si from wollastonite, and Al

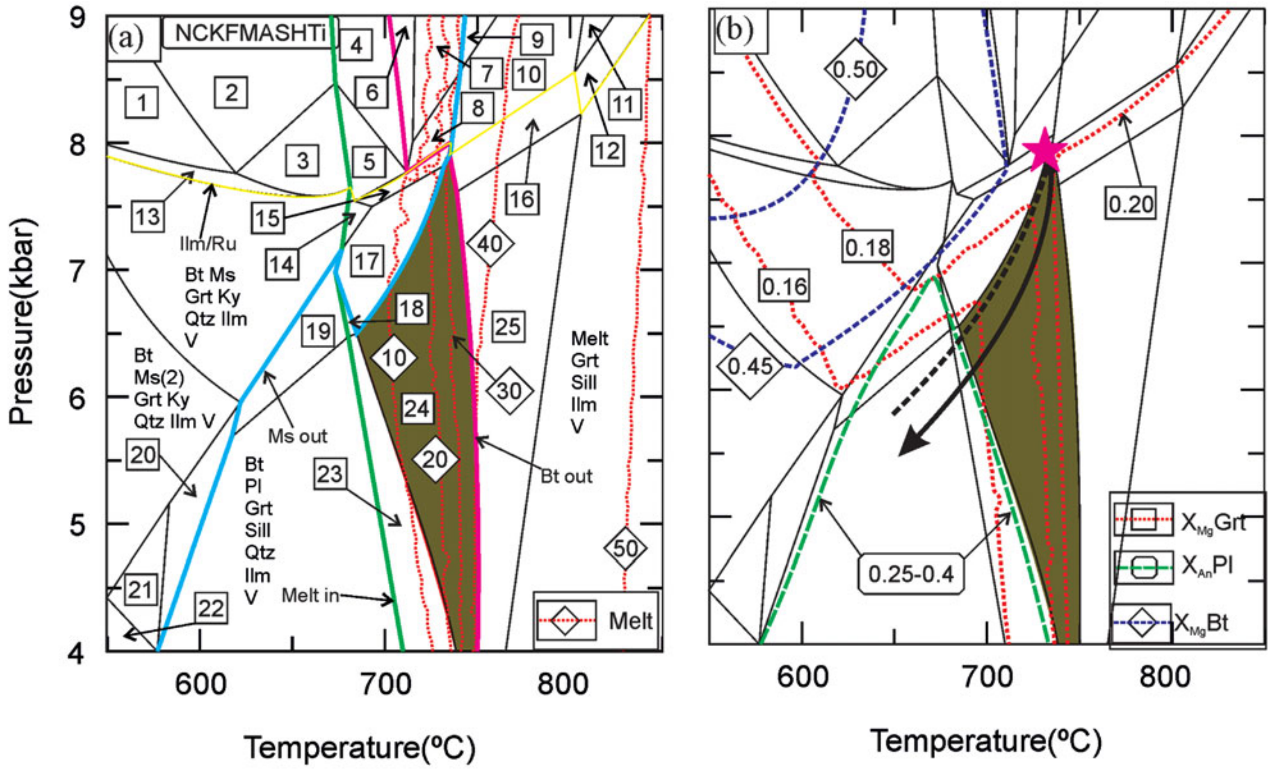

1: Bt Ms Grt Ky Qtz Ru V
2: Bt Ms Grt Qtz Ru V
3: Bt Ms Grt Qtz Ru Ilm V
4: Bt Melt Ms Grt Qtz Ru V
5: Bt Melt Ms Grt Qtz Ru Ilm V
6: Melt Ms Grt Qtz Ru V
7: Melt Ms Grt Ky Qtz Ru V
8: Melt Ms Grt Sill Qtz Ru V
9: Melt Grt Ky Qtz Ru V
10: Melt Grt Sill Qtz Ru V
11: Melt Grt Sill Ru V
12: Melt Grt Sill Ru Ilm V
13: Bt Ms Grt Ky Qtz Ru Ilm V
14: Bt Melt Ms Grt Ky Qtz Ilm V
15: Bt Melt Ms Grt Sill Qtz Ru Ilm V
16: Melt Grt Sill Qtz Ru Ilm V
17: Bt Melt Ms Grt Sill Qtz Ilm V
18: Bt Melt Pl Ms Grt Sill Qtz Ilm V
19: Bt Pl Mica Grt Sill Qtz Ilm V
20: Bt Ms Grt Sill Qtz Ilm V
21: Bt Ms(2) Grt Sill Qtz Ilm V
22: Bt Ms(2) Grt And Qtz Ilm V
23: Bt Melt Pl Grt Sill Qtz Ilm V
24: Bt Melt Grt Sill Qtz Ilm V
25: Melt Grt Sill Qtz Ilm V

Figure 7. (Colour online) (a) Pseudosections in NCKFMASHTi system from bulk composition of mesocratic domain of BJ-30. The bulk composition in mol. % is $SiO_2 = 54.57$, $TiO_2 = 1.45$, $Al_2O_3 = 13.29$, $FeO = 21.89$, $MgO = 5.36$, $CaO = 1.41$, $Na_2O = 0.16$, $K_2O = 1.23$ and $H_2O = 20.39$. Melt abundance is shown as isopleths. (b) Compositional isopleths of garnet, biotite and feldspar in the *P–T* pseudosection of (a).

from Al_2O_3. All errors are given as 2σ. Weighted isochrons and deconvolution histograms were calculated using Isoplot 4.15 (Ludwig 2001).

Almost 100 spots were analysed in *c.* 40 crystals from two migmatite samples; analytical data for the dated monazites are shown in Table 4. While sample BJ-30 contains a simple population of monazites with ages around 1740 Ma the other sample BJ-28 is more complicated, showing at least two populations (*c.* 1740 and 800 Ma). The six spots with apparent ages between 1100 and 1400 Ma are interpreted as mixed ages of the spots between old and young domains. The monazites from BJ-30 (n = 27 points) give a weighted mean age of 1741 ± 7 Ma or U/Pb v. Th/Pb isochron centroid age of 1746 ± 14 Ma (Cocherie & Albarede, 2001). The increased value of MSWD = 3.6 indicates that the U–Th–Pb system was partly disturbed, as indicated by the presence of three spots with higher ages 1780–1827 Ma. Omitting these spots the isochron gives an age of 1739 ± 9 Ma with MSWD 1.7 (Fig. 9). Both isochrons are concordant. The monazites from the other sample BJ-28 record more than one event. Dating yielded two apparent ages, higher at *c.* 1700 Ma and lower at *c.* 780 Ma. The older monazites form centres of crystals forming their dominant part. The U/Pb v. Th/Pb isochron gives a centroid age of 1688 ± 25 Ma, but a high MSWD = 11 indicates disturbance of the system, presumably due to younger overprint.

The lower ages are found at the rims of larger grains; some small monazites show only the lower age (mnz 5, 21, both enclosed in muscovite). The weighted average is 782 ± 13 Ma for n = 24 spots and a high MSWD = 7.5. A similar age is also obtained from the U/Pb v. Th/Pb isochron (788 ± 20 Ma). The apparently inhomogeneous population may involve domains with mixed ages as shown by the deconvolution histogram (Fig. 10).

Table 3a. Garnet–biotite thermometry at reference pressure 8 kbar

	Bhattacharya *et al.* (1992)	Dasgupta *et al.* (1991)	Ferry & Spear (1978)	Holland & Powell (1998)	Holdaway (2000)	Average (Grt–Bt)
BJ-28						
Grt (C)–Bt (I)	512 °C	428 °C	491 °C	526° C	576 °C	507 °C
	509 °C	420 °C	486 °C	515 °C	572 °C	500 °C
	519 °C	429 °C	507 °C	541 °C	585 °C	516 °C
Grt (E^Bt)–Bt(M-R^Grt)	515 °C	400 °C	513 °C	520 °C	587 °C	507 °C
	540 °C	431 °C	551 °C	570 °C	606 °C	540 °C
	552 °C	458 °C	570 °C	603 °C	616 °C	560 °C
BJ-30						
Grt (C)–Bt(I)	514 °C	476 °C	481 °C	502 °C	571 °C	509 °C
	506 °C	468 °C	473 °C	486 °C	566 °C	500 °C
Grt (OR)–Bt(I)	510 °C	466 °C	470 °C	493 °C	563 °C	500 °C
Grt (E^Bt)–Bt(M-R^Grt)	515 °C	460 °C	472 °C	513 °C	563 °C	505 °C
	512 °C	459 °C	466 °C	506 °C	560 °C	501 °C
	520 °C	482 °C	484 °C	515 °C	572 °C	515 °C

I – inclusion; M – matrix; C – core; E – edge; OR – outer rim; R – rim; ^ – against.

Table 3b. Titanium-in-biotite thermometry after Henry, Guidotti & Thomson (2005)

BJ-28			BJ-30		
Grain-1	C	666 °C		M(C)	741 °C
	M(R^Grt)	672 °C			741 °C
	M(R^Ms-Qtz)	663 °C			746 °C
Grain-2	M(C)	649 °C	Grain-1	M(C)	754 °C
	M(R^Grt)	638 °C		M(R^Grt)	752 °C
Grain-3	M(C)	662 °C		M(R^Grt)	735 °C
	M(R^Grt)	642 °C			737 °C
					754 °C
Grain-4	M(C)	638 °C		I^Grt (C)	743 °C
	M(R^Grt)	655 °C			764 °C
Grain-5	M(R^Grt)	636 °C		I^Grt (OR)	761 °C
	I^Grt (C)	655 °C		S^Kfs(L)	746 °C
		638 °C			
		659 °C			
		646 °C			

I – inclusion; M – matrix; C – core; S – symplectite; OR – outer rim; ^ – against; L – leucosome.

5. Discussion

5.a. *P–T* conditions of crustal anatexis

To constrain the *P–T* conditions of partial melting in the migmatites, we carried out pseudosection analyses using the hypothetical bulk metapelite composition of White, Powell & Holland (2001; Fig. 5a–d). The results of the pseudosection analyses are compared with those obtained from the *P–T* pseudosections computed using the bulk compositions of mesocratic layers in the samples (Figs 6a, b, 7a).

Isopleth thermometry from the bulk composition of BJ-30 yields a T_{Max} of $\sim$750 °C at 8 kbar necessary for garnet stability (Fig. 7b). The result is similar to the corresponding value obtained from the pseudosection analyses from the hypothetical metapelite bulk composition of White, Powell & Holland (2001) and from titanium-in-biotite thermometry (Table 3b). The maximum temperature obtained from the isopleth thermometry of the biotite composition in Figure 5b, d is $\sim$800 °C, $\sim$50 °C higher than that obtained from garnet thermometry ($\sim$750 °C). Hence, we conclude that the *P–T* conditions for stability of the peak assemblage garnet + sillimanite + biotite + quartz + feldspar + melt were $\sim$8 kbar and 750–800 °C. Textural observations from BJ-30 indicate that biotite–sillimanite–quartz inclusions in the garnet (Fig. 4c) were the phases participating in the prograde reactions. On the other hand, matrix biotite, sillimanite and quartz (Fig. 4c–h) formed during retrogression. Thus, we propose a clockwise *P–T* path (tight-loop) with decompression during retrogression (Fig. 7b). A decrease in pressure to $\sim$6.5 kbar is derived from the intersection of garnet isopleths with X_{An} isopleths of plagioclase occurring in the garnet fractures (Fig. 7b; Table 1c).

Pseudosection analyses from the BJ-28 bulk composition indicate stability of the muscovite–biotite–garnet–quartz–feldspar–melt-bearing peak assemblage in water-undersaturated conditions at $\sim$700 °C and above 6.5 kbar pressure (Fig. 6a). Although the temperature estimated from the isopleth thermometry is in agreement with that obtained from titanium-in-biotite thermometry (Table 3b), it is about $\sim$100–150 °C higher than that predicted from the garnet–biotite thermometry ($\sim$500–560 °C; Table 3a).

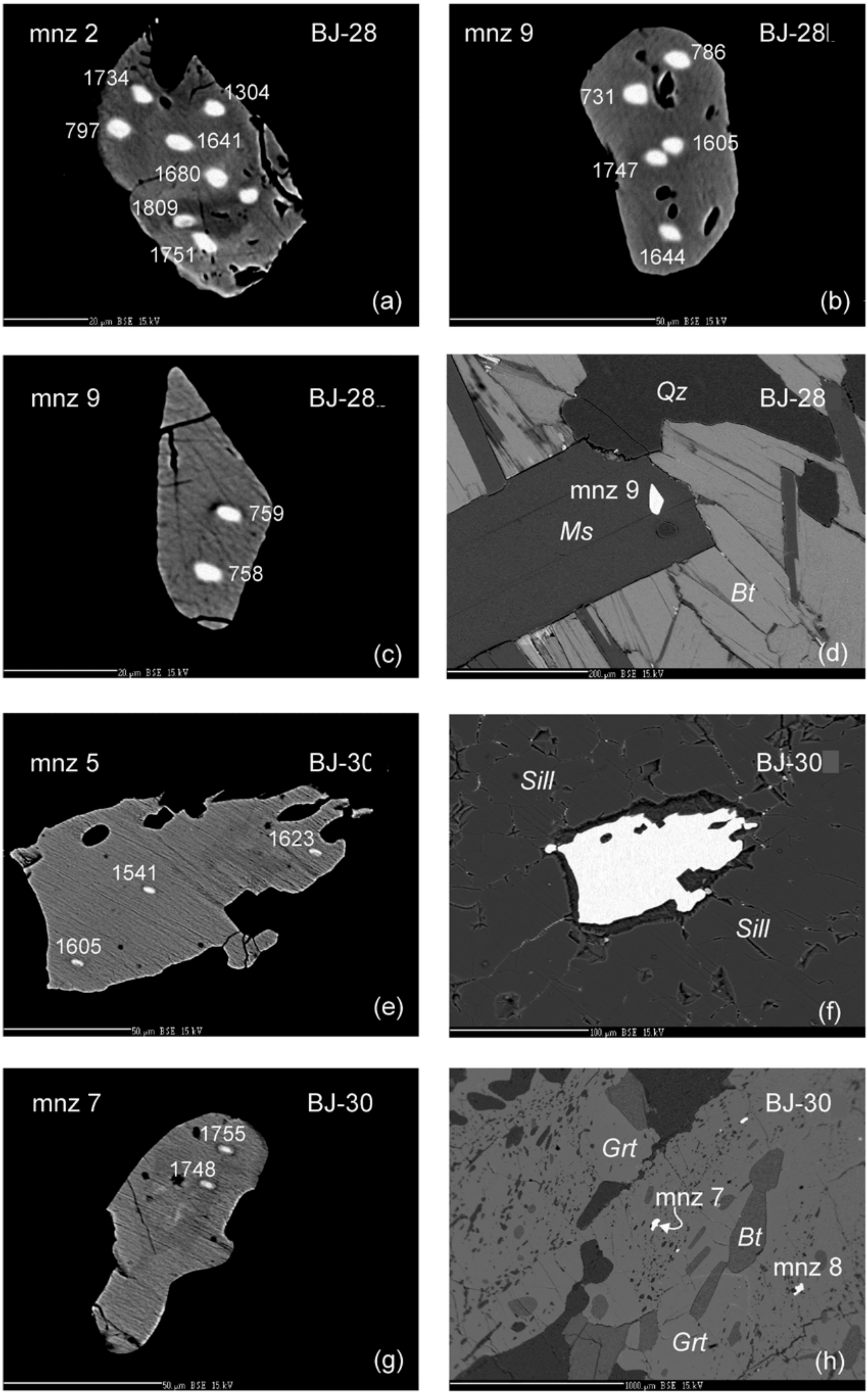

Figure 8. BSE images of the dated monazites and their enclosing minerals.

Table 4. Analytical data for the dated monazites (samples BJ-28, BJ-30)

sample	grain	Th	U	Pb	Y	Ucorr	Pbcorr	Th 2 sigma	U 2 sigma	Pb 2 sigma	age Ma	age 2 s	Th*
BJ-30	mnz1/1	5.565	0.370	0.464	0.252	0.305	0.460	0.036	0.013	0.007	1502	35.4	6.66
BJ-30	mnz1/2	6.068	0.290	0.553	0.089	0.220	0.551	0.037	0.012	0.007	1732	37.3	6.88
BJ-30	mnz2/1	5.869	0.390	0.367	0.284	0.322	0.362	0.037	0.013	0.007	1136	30.1	6.99
BJ-30	mnz2/2	6.470	0.270	0.306	0.183	0.195	0.300	0.038	0.012	0.006	928	27.2	7.13
BJ-30	mnz2/3	6.026	0.321	0.524	0.081	0.251	0.522	0.037	0.013	0.007	1630	35.8	6.94
BJ-30	mnz3/1	6.215	0.291	0.561	0.103	0.219	0.559	0.038	0.013	0.008	1720	36.8	7.02
BJ-30	mnz3/2	5.725	0.312	0.543	0.115	0.246	0.542	0.036	0.013	0.007	1763	38.6	6.63
BJ-30	mnz3/3	5.888	0.458	0.573	0.179	0.389	0.571	0.037	0.013	0.008	1689	34.9	7.32
BJ-30	mnz4/1	6.229	0.292	0.562	0.079	0.220	0.560	0.038	0.013	0.008	1721	36.7	7.04
BJ-30	mnz4/2	5.585	0.285	0.512	0.064	0.220	0.511	0.036	0.012	0.007	1726	39.5	6.40
BJ-30	mnz4/3	5.414	0.287	0.490	0.049	0.224	0.489	0.035	0.012	0.007	1697	39.8	6.24
BJ-30	mnz5/1	5.993	0.331	0.517	0.119	0.262	0.514	0.037	0.013	0.007	1605	35.6	6.95
BJ-30	mnz5/2	6.351	0.513	0.566	0.151	0.440	0.563	0.038	0.013	0.008	1541	31.6	7.94
BJ-30	mnz5/3	5.863	0.287	0.501	0.078	0.219	0.499	0.037	0.012	0.007	1623	36.9	6.66
BJ-30	mnz6/1	5.239	0.702	0.642	2.115	0.642	0.620	0.035	0.014	0.008	1763	34.9	7.61
BJ-30	mnz6/2	5.760	0.463	0.586	0.166	0.396	0.584	0.036	0.013	0.008	1747	36.0	7.22
BJ-30	mnz6/3	5.338	0.621	0.626	2.186	0.559	0.603	0.035	0.014	0.008	1762	35.7	7.41
BJ-30	mnz7/1	5.838	0.567	0.631	0.672	0.499	0.623	0.037	0.014	0.008	1755	34.6	7.68
BJ-30	mnz7/2	5.087	0.922	0.685	1.831	0.863	0.667	0.034	0.015	0.008	1748	32.6	8.27
BJ-30	mnz8/1	7.603	0.267	0.703	1.043	0.179	0.690	0.042	0.012	0.008	1799	33.7	8.27
BJ-30	mnz8/2	5.279	0.713	0.645	1.776	0.652	0.627	0.035	0.014	0.008	1765	34.6	7.69
BJ-30	mnz8/3	5.813	0.537	0.619	0.603	0.470	0.612	0.037	0.013	0.008	1754	34.9	7.55
BJ-30	mnz9/1	5.355	0.264	0.514	0.927	0.201	0.503	0.035	0.012	0.007	1781	41.7	6.10
BJ-30	mnz9/2	5.643	0.517	0.604	0.520	0.451	0.598	0.036	0.013	0.008	1768	35.9	7.31
BJ-30	mnz10/1	5.899	0.472	0.600	0.422	0.403	0.595	0.037	0.013	0.008	1742	35.2	7.39
BJ-30	mnz10/2	5.957	0.388	0.580	0.279	0.319	0.576	0.037	0.013	0.008	1745	36.2	7.13
BJ-30	mnz11/1	5.915	0.292	0.470	0.065	0.224	0.468	0.037	0.012	0.007	1513	35.3	6.72
BJ-30	mnz11/2	6.020	0.483	0.603	0.159	0.413	0.601	0.037	0.013	0.008	1723	34.6	7.54
BJ-30	mnz11/3	5.230	0.897	0.700	2.012	0.836	0.680	0.035	0.015	0.008	1767	32.7	8.33
BJ-30	mnz12/1	5.247	0.960	0.706	1.980	0.899	0.686	0.035	0.015	0.008	1736	31.6	8.57
BJ-30	mnz12/2	5.822	0.495	0.605	0.485	0.428	0.600	0.036	0.013	0.008	1752	35.4	7.40
BJ-30	mnz13/1	5.135	0.681	0.651	2.099	0.622	0.630	0.034	0.014	0.008	1827	35.9	7.45
BJ-30	mnz13/2	5.861	0.562	0.623	0.621	0.494	0.616	0.037	0.014	0.008	1734	34.2	7.68
BJ-30	mnz14/1	5.845	0.560	0.621	0.610	0.492	0.614	0.037	0.013	0.008	1735	34.3	7.66
BJ-30	mnz14/2	5.001	0.599	0.567	1.804	0.541	0.548	0.034	0.013	0.007	1699	35.9	6.99
BJ-30	mnz14/3	4.789	0.615	0.566	1.896	0.560	0.547	0.033	0.014	0.008	1728	37.1	6.85
BJ-28	mnz1/1	4.719	0.630	0.512	1.879	0.575	0.493	0.041	0.013	0.007	1574	36.5	6.80
BJ-28	mnz1/2	5.846	0.945	0.301	1.556	0.877	0.281	0.048	0.015	0.006	711	21.4	8.79
BJ-28	mnz2/1	1.180	0.183	0.157	0.774	0.169	0.151	0.020	0.012	0.006	1809	110.2	
BJ-28	mnz2/2	6.340	0.235	0.549	0.849	0.161	0.538	0.051	0.012	0.008	1680	38.2	6.93
BJ-28	mnz2/3	5.930	0.519	0.586	1.163	0.450	0.573	0.049	0.013	0.008	1641	35.0	7.57
BJ-28	mnz2/4	4.915	0.758	0.279	1.439	0.701	0.262	0.042	0.014	0.006	797	25.5	7.28
BJ-28	mnz3/1	5.375	0.570	0.558	1.204	0.508	0.546	0.045	0.013	0.008	1637	35.8	7.23
BJ-28	mnz4/1	4.706	0.566	0.534	2.111	0.511	0.512	0.041	0.013	0.007	1688	38.7	6.58
BJ-28	mnz4/2	4.586	0.892	0.283	1.778	0.838	0.262	0.041	0.014	0.006	785	25.2	7.41
BJ-28	mnz5/1	4.711	0.954	0.286	1.802	0.899	0.265	0.041	0.015	0.006	760	24.2	7.74
BJ-28	mnz6/1	4.330	1.160	0.632	1.840	1.110	0.615	0.039	0.015	0.008	1599	31.4	8.36
BJ-28	mnz6/2	4.578	0.689	0.553	2.222	0.635	0.530	0.041	0.014	0.008	1666	37.1	6.90
BJ-28	mnz7/1	3.037	1.027	0.233	1.924	0.991	0.213	0.031	0.015	0.006	743	28.0	6.37
BJ-28	mnz7/2	3.335	0.947	0.227	1.767	0.909	0.208	0.033	0.015	0.006	726	27.6	6.38
BJ-28	mnz8/1	5.747	0.197	0.503	0.765	0.130	0.494	0.047	0.012	0.007	1715	41.7	6.23
BJ-28	mnz8/2	5.833	0.432	0.560	1.037	0.364	0.548	0.048	0.013	0.008	1657	36.6	7.17
BJ-28	mnz8/3	5.137	1.005	0.311	1.893	0.946	0.289	0.044	0.015	0.007	770	23.2	8.32
BJ-28	mnz9/1	4.540	0.603	0.505	2.084	0.551	0.483	0.040	0.013	0.007	1605	38.1	6.54
BJ-28	mnz9/2	5.100	1.033	0.295	1.665	0.973	0.275	0.044	0.015	0.006	731	22.4	8.37
BJ-28	mnz2/5	5.4678	0.8030	0.6752	1.8873	0.7396	0.6560	0.0356	0.0146	0.0080	1734	32.9	8.20
BJ-28	mnz2/6	5.2441	0.8180	0.4909	1.7601	0.7572	0.4716	0.0348	0.0146	0.0072	1304	29.1	7.92
BJ-28	mnz2/7	6.7509	0.2306	0.6037	0.8527	0.1523	0.5928	0.0394	0.0122	0.0077	1751	36.1	7.31
BJ-28	mnz5/2	4.9810	1.0579	0.3166	2.0665	1.0001	0.2927	0.0341	0.0157	0.0066	778	23.0	8.35
BJ-28	mnz5/3	5.0410	1.0172	0.3106	2.1418	0.9587	0.2858	0.0342	0.0155	0.0065	767	23.0	8.27
BJ-28	mnz5/4	4.8090	0.9848	0.3358	1.7968	0.9290	0.3153	0.0334	0.0153	0.0066	877	24.7	7.96
BJ-28	mnz6/3	4.7007	0.6355	0.6197	2.4643	0.5810	0.5950	0.0329	0.0137	0.0077	1868	38.3	6.88
BJ-28	mnz6/4	4.7630	0.9248	0.2992	1.8028	0.8696	0.2784	0.0332	0.0151	0.0065	802	24.6	7.70
BJ-28	mnz6/5	4.7201	0.8068	0.4811	1.8018	0.7520	0.4622	0.0331	0.0145	0.0072	1367	31.4	7.39
BJ-28	mnz9/3	5.3770	1.0128	0.3251	1.7584	0.9504	0.3040	0.0353	0.0155	0.0066	786	22.5	8.58
BJ-28	mnz9/4	4.3767	0.5844	0.5356	2.3016	0.5336	0.5124	0.0319	0.0135	0.0074	1747	39.4	6.35
BJ-28	mnz9/5	4.9147	0.8509	0.6152	2.3283	0.7939	0.5916	0.0337	0.0147	0.0077	1644	32.9	7.81
BJ-28	mnz10/1	5.1911	0.8439	0.6706	2.3565	0.7837	0.6468	0.0347	0.0147	0.0079	1734	33.0	8.08
BJ-28	mnz10/2	5.2510	0.7124	0.3202	1.5243	0.6515	0.3018	0.0347	0.0141	0.0066	894	26.2	7.47
BJ-28	mnz10/3	5.0810	0.9341	0.3182	1.9547	0.8752	0.2954	0.0343	0.0151	0.0066	815	24.0	8.04
BJ-28	mnz11/1	11.2480	1.2242	0.5812	1.7742	1.0937	0.5525	0.0522	0.0165	0.0075	819	15.1	14.95
BJ-28	mnz11/2	21.4550	1.0976	1.0362	1.3169	0.8487	0.9998	0.0778	0.0163	0.0093	906	11.6	24.35
BJ-28	mnz11/3	8.3290	0.9419	0.4349	2.1731	0.8453	0.4054	0.0442	0.0153	0.0070	803	18.5	11.18
BJ-28	mnz12/1	11.5570	1.1131	0.5717	1.7430	0.9790	0.5428	0.0530	0.0158	0.0075	809	15.0	14.86

Table 4. Continued

sample	grain	Th	U	Pb	Y	Ucorr	Pbcorr	Th 2 sigma	U 2 sigma	Pb 2 sigma	age Ma	age 2 s	Th*
BJ-28	mnz12/2	22.8371	0.9200	1.3024	1.5899	0.6551	1.2634	0.0809	0.0155	0.0102	1105	12.6	25.11
BJ-28	mnz12/3	5.5380	0.9298	0.3188	2.1346	0.8656	0.2933	0.0358	0.0151	0.0066	770	22.7	8.45
BJ-28	mnz13/1	9.9407	0.2189	0.8923	0.7892	0.1036	0.8796	0.0487	0.0123	0.0088	1835	29.3	10.33
BJ-28	mnz13/2	4.8802	0.9377	0.4538	1.7435	0.8811	0.4350	0.0336	0.0150	0.0071	1200	27.9	7.96
BJ-28	mnz14/1	4.7878	0.9195	0.6474	1.5712	0.8640	0.6325	0.0333	0.0151	0.0079	1721	33.1	7.97
BJ-28	mnz14/2	4.9000	0.9279	0.3043	1.8594	0.8711	0.2827	0.0337	0.0151	0.0065	800	24.4	7.84
BJ-28	mnz15/1	6.2043	0.7954	0.7411	1.4398	0.7234	0.7262	0.0379	0.0145	0.0082	1769	31.3	8.88
BJ-28	mnz15/2	5.5420	0.9524	0.3291	1.7635	0.8881	0.3077	0.0357	0.0152	0.0066	799	22.7	8.54
BJ-28	mnz16/1	5.1805	1.5649	0.8770	2.1021	1.5048	0.8580	0.0347	0.0181	0.0087	1735	27.4	10.73
BJ-28	mnz16/2	5.3230	1.0130	0.3365	2.0971	0.9512	0.3119	0.0351	0.0155	0.0067	810	22.9	8.54
BJ-28	mnz17/1	5.1667	0.7611	0.6299	1.2785	0.7012	0.6174	0.0345	0.0143	0.0078	1726	33.9	7.75
BJ-28	mnz17/2	5.1220	1.0108	0.3264	2.0558	0.9514	0.3025	0.0344	0.0155	0.0066	805	23.2	8.33
BJ-28	mnz18/1	4.7598	1.0665	0.6868	1.6874	1.0113	0.6711	0.0333	0.0157	0.0080	1716	31.6	8.48
BJ-28	mnz18/2	4.8598	0.8894	0.6417	2.0267	0.8330	0.6217	0.0335	0.0149	0.0078	1702	33.0	7.92
BJ-28	mnz19/1	7.0890	0.6847	0.7483	1.5913	0.6025	0.7303	0.0399	0.0139	0.0081	1700	29.3	9.30
BJ-28	mnz19/2	5.1570	1.0186	0.3170	2.0768	0.9588	0.2927	0.0339	0.0152	0.0065	775	22.5	8.39
BJ-28	mnz20/1	4.9737	0.8166	0.6474	2.5157	0.7589	0.6220	0.0340	0.0145	0.0079	1734	34.0	7.77
BJ-28	mnz20/2	5.0297	0.8611	0.5608	2.3901	0.8028	0.5358	0.0341	0.0147	0.0075	1477	31.0	7.91
BJ-28	mnz20/3	5.0622	0.6831	0.4525	1.2692	0.6244	0.4385	0.0341	0.0139	0.0071	1320	31.1	7.27
BJ-28	mnz20/4	6.1510	0.7964	0.2189	1.6617	0.7251	0.1964	0.0375	0.0145	0.0062	513	19.8	8.54
BJ-28	mnz21/1	5.2180	1.0398	0.3143	1.9851	0.9793	0.2909	0.0349	0.0157	0.0066	759	22.5	8.51
BJ-28	mnz21/2	5.0210	1.0047	0.3031	1.9867	0.9465	0.2799	0.0335	0.0151	0.0063	758	22.5	8.20
BJ-28	mn22/1	5.1321	1.4533	0.8040	2.0297	1.3938	0.7851	0.0339	0.0172	0.0083	1667	27.1	10.24
BJ-28	mn22/2	5.2383	0.7355	0.6255	1.5385	0.6747	0.6100	0.0347	0.0142	0.0077	1712	33.7	7.72

Notes: The units in the table are wt. % (Th, U, Y, Pb). Pbcorr, Ucorr values corrected against standards, for details see methods. Th* equivalent Th, errors are 2 sigma.

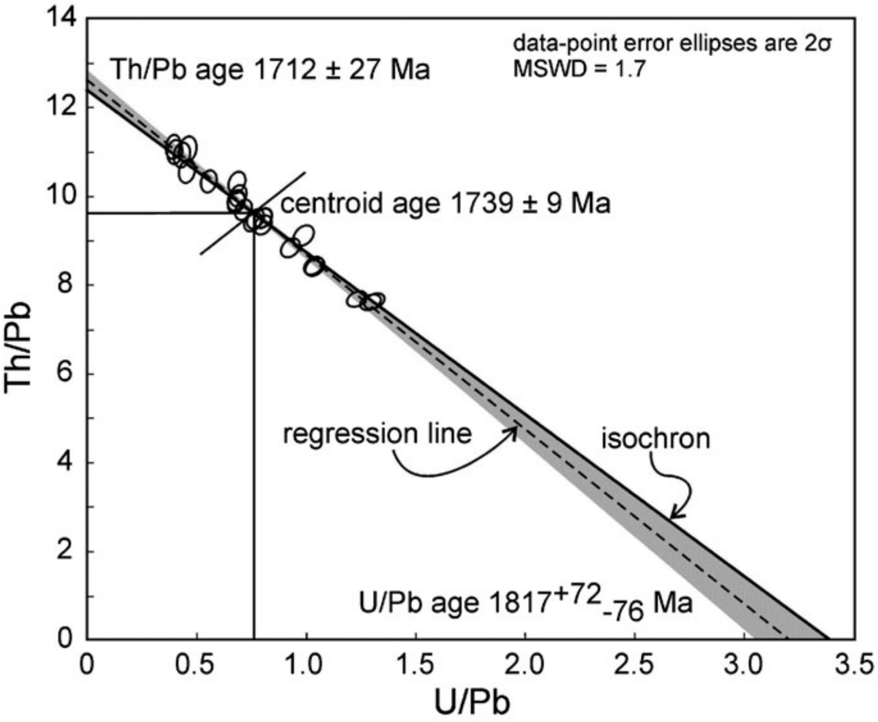

Figure 9. U/Pb–Th/Pb isochron ages of monazites from sample BJ-30.

A lower temperature range for garnet–biotite thermometry (using conventional thermometers and THERMOCALC) as compared to the single element titanium-in-biotite thermometer and isopleths thermometry is attributed to compositional resetting between garnet and biotite during post-peak cooling in the presence of melt. Hence, the minimum temperature predicted for retrogression was ~500 °C. However, owing to compositional homogeneity of the phases it is difficult to estimate whether the post-peak cooling was isobaric or accompanied by decompression.

5.b. Late Palaeoproterozoic anatexis in the gneisses

Metamorphic monazites in the foliation domains in garnet–biotite–muscovite gneiss (BJ-28) occurring in the eastern part of the study area yield two age

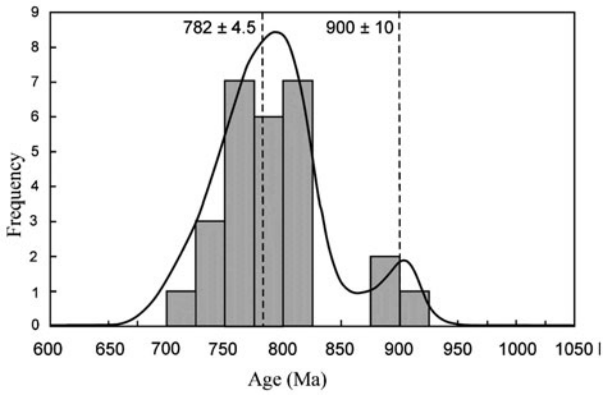

Figure 10. Histogram of the monazite ages from sample BJ-28.

populations, i.e. monazite cores ~1.74 Ga, and monazite rims ~0.8 Ga (Figs 9, 10). In the biotite–sillimanite–garnet-bearing gneiss (BJ-30) in the southwestern part, monazites in the matrix as well as monazites sequestered in garnet porphyroblasts (Figs 8e, f) yield a single, well-constrained age population of ~1.73 Ga (Fig. 9). The ~1.73 Ga age coincides with the timing of mid-crustal anatexis and charnockite emplacement in the SC, and A-type granite magmatism in the NDFB (Roy *et al.* 2005; Buick *et al.* 2006; Saha *et al.* 2008; Kaur *et al.* 2011*a,b*). Evidently, anatexis in the gneisses in the eastern part of the ADFB was contemporaneous with the Late Palaeoproterozoic high-grade metamorphism and felsic magmatism reported in the western part of the ADFB. This work, therefore, provides a framework to demonstrate that the ~1.8–1.7 Ga high-grade metamorphism recorded in the BGC-II comprising the Sandmata and the Mangalwar complexes is not restricted to the west of the Delwara Lineament, but extends within the anatectic gneisses of the Aravalli Supergroup until the Jahazpur Belt (Figs 1b, 2). Hence, the BGC-II and the anatectic gneisses of the Aravalli Supergroup (of Roy & Jakhar, 2002) shared a common tectono-metamorphic history in Late Palaeoproterozoic time.

The rarity of 1.0–0.9 Ga ages – obtained in a couple of spots on monazite grains (Fig. 9) – in the two anatectic gneisses, suggests the effect of Grenvillian-age tectonics is prominent in the Sandmata and the Mangalwar complexes in the western part of the ADFB and along the Delwara Lineament but does not extend eastwards of Pur–Banera (Buick *et al.* 2006, 2010; Bhowmik, Bernhardt & Dasgupta, 2010; Hazarika, Upadhyay & Mishra, 2013; Ozha *et al.* 2015). The Neoproterozoic monazite chemical ages (~780–800 Ma) in the rims of the monazites in BJ-28 are similar to the ages of the felsic volcanic rocks in the Malani Igneous Suite (~770 Ma) in the Marwar Craton in the west of the ADFB (Gregory *et al.* 2009). This age population is lacking in BJ-30. However, we are unable to correlate these monazite growth ages with any particular metamorphic/deformation event. The interpretation of the Neoproterozoic ages, therefore, remains uncertain, and needs further investigation. It is possible that the monazite chemical age in BJ-28 located close to the Hindoli Group, but lacking in BJ-30, may correspond with the Jahazpur thrust or a younger reactivation event along the thrust.

5.c. Inconsistencies in monazite ages in the Aravalli Craton

The present study demonstrates that the ~1.7 Ga high-grade metamorphism in the BGC-II (Wiedenbeck, Goswami & Roy, 1996 *b*; Roy *et al.* 2005; Buick *et al.* 2006) is not restricted to the west of the Delwara Lineament but extends eastwards within the expansive anatectic gneisses of the Aravalli Supergroup. This implies that the BGC-II and the anatectic gneisses of the Aravalli Supergroup shared a common tectono-metamorphic history since Late Palaeoproterozoic time. In this context, the monazite chemical ages reported in the supracrustal belts of Pur–Banera (Ozha *et al.* 2016), Rajpura–Dariba and Rampura–Agucha (Hazarika, Upadhyay & Mishra, 2013) lead to several contradictions. In the Pur–Banera Complex, Ozha *et al.* (2016) correlate three metamorphic stages (M_1 (peak *P–T* at ~5.5 kbar, 520–550 °C), M_2 (peak *P–T* at ~7.5 kbar and 580–660 °C) and M_3 (with peak *P–T* at ~8.0 kbar and 590–640 °C)) with monazite chemical ages at ~1.82 Ga, 1.35–1.37 Ga and ~1.0 Ga, respectively. On the other hand, in the Rajpura–Dariba supracrustal rocks, monazite chemical ages are populated at ~1.62 Ga and ~1.87 Ga only; the authors correlate the more populous older age cluster with the ~1.8 Ga Pb–Pb age reported by Deb *et al.* (1989) for syn-sedimentary sulfide mineralization in the supracrustal rocks. By contrast in the Rampura–Agucha anatectic gneisses (Hazarika, Upadhyay & Mishra, 2013), the mean values of the overwhelmingly large number of chemical spot ages in three monazite-dated samples occur at 1006 ± 13 Ma (AM-370/3), 1041 ± 14 Ma (AM-5) and 1004 ± 12 Ma (AM-370/12A); in the samples, minor age populations occur at ~1.36 Ga, ~1.66 Ga (AM-370/3) and ~1.57 Ga (AM-5). Based on the data, the authors suggest that the Rampura–Agucha supracrustal rocks experienced two amphibolite-facies tectono-thermal events, the older event at ~1.6 Ga (largely obliterated) and the younger high-grade metamorphism at ~1.0 Ga.

Assuming that the polymetamorphism invoked by the authors is induced by regional tectono-thermal events, unless conclusive evidence of local heat sources (heat release from younger magma emplacements, and heating induced by brittle/ductile shearing) proves to the contrary, several inconsistencies are evident in the monazite age data. Notable among these are: (i) the ~1.3 Ga amphibolite-facies M_2 metamorphic event recorded in Pur–Banera is lacking in the Rajpura–Dariba supracrustal belt, and in the Deoli–Shahpura anatectic gneisses that arguably form the basement for the supracrustal belts, and also in the BGC-II; (ii) the ~1.7–1.6 Ga tectono-metamorphic event lacking in Pur–Banera is recorded in the BGC-II, the Deoli–Shahpura anatectic gneisses (this study), and in the supracrustal rocks of Rajpura–Dariba and Rampura–Agucha; and (iii) the expansive ~1.7 Ga metamorphism in the BGC-II and the Deoli–Shahpura migmatite gneisses occurred at anatectic conditions, but the Rajpura–Dariba lithologies overlying the gneisses reached middle-amphibolite-facies conditions. Several lines of evidence may suggest that the supracrustal belts may have been tectonically accreted to the basement gneisses or were deposited on the basement gneisses post ~1.3 Ga, and deformed-metamorphosed subsequently at ~1.0 Ga, e.g. (i) the lack of ~1.3 Ga metamorphic monazite in the supracrustal belts (barring Pur–Banera) and in the anatectic gneisses of the Aravalli Supergroup, and (ii) the prevalence of ~1.7 Ga metamorphic monazites in the Aravalli Supergroup and the lack of this age in Pur–Banera. In the former case (tectonic accretion), the pre-Grenvillian monazites are likely to record pre-accretionary metamorphism in the allochthonous block; in the second case (deposition on gneiss basement), the >1.0 Ga monazites possibly qualify as detrital grains of igneous/metamorphic origin inherited from the source rocks. A critical structural analysis of the basement–cover relationships in the supracrustal belts, combined with robust age determination to ascertain the time of accretion/deposition of the supracrustal belts is likely to distinguish between the two possible scenarios in the ADFB.

Acknowledgements. LS acknowledges the Faculty Initiation Grant 2013, sponsored by IIT Roorkee for conducting field trips and analyses. This research was also financially supported by the Slovak Research and Development Agency (projects APVV-0080-11 to MJ and APVV-14-0278 to IP), and the Slovak Scientific Grant Agency VEGA (projects 2/0060/16 to MJ and 2/0067/16 to IP). The authors acknowledge two anonymous reviewers for their suggestions which helped to improve the scientific content of the manuscript.

References

AUZANNEAU, E., SCHMIDT, M. W., VIELZEUF, D. & CONNOLLY, J. A. D. 2010. Titanium in phengite: a geobarometer for high temperature eclogites. *Contributions to Mineralogy and Petrology* **159**, 1–24.

BENISEK, A., DACHS, E. & KROLL, H. 2010. A ternary feldspar-mixing model based on calorimetric data: development and application. *Contributions to Mineralogy and Petrology* **160**, 327–37.

BHATTACHARYA, A., MOHANTY, L., MAJI, A., SEN, S. K. & RAITH, M. 1992. Non-ideal mixing in the phlogopite-annite boundary: constraints from experimental data on Mg-Fe partitioning and a reformulation of the biotite-garnet geothermometer. *Contributions to Mineralogy and Petrology* **111**, 87–93.

BHOWMIK, S. K., BERNHARDT, H.-J. & DASGUPTA, S. 2010. Grenvillian age high pressure upper amphibolite–granulite metamorphism in the Aravalli–Delhi Mobile Belt, Northwestern India: new evidence from monazite chemical age and its implication. *Precambrian Research* **78**, 168–84.

BHOWMIK, S. K. & DASGUPTA, S. 2012. Tectonothermal evolution of the Banded Gneissic Complex in central Rajasthan, NW India: present status and correlation. *Journal of Asian Earth Sciences* **49**, 339–48.

BIJU-SEKHAR, S., YOKOYAMA, K., PANDIT, M. K., OKUDAIRA, T., YOSHIDA, M. & SANTOSH, M. 2003. Late Paleoproterozoic magmatism in Delhi Fold Belt, NW India and its implication: evidence from EPMA chemical ages of zircons. *Journal of Asian Earth Sciences* **22**, 189–207.

BOSE, U. & SHARMA, A. K. 1992. The volcanic sedimentary association of the Precambrian Hindoli Supracrustals in south-east Rajasthan. *Journal of the Geological Society of India* **40**, 359–69.

BUICK, I. S., ALLEN, C., PANDIT, M., RUBATTO, D. & HERMANN, J. 2006. The Proterozoic magmatic and metamorphic history of the Banded Gneiss Complex, central Rajasthan, India: LA-ICP-MS U–Pb zircon constraints. *Precambrian Research* **151**, 119–42.

BUICK, I. S., CLARK, C., RUBATTO, D., HERMANN, J., PANDIT, M. K. & HAND, M. 2010. Constraints on the Proterozoic evolution of the Aravalli–Delhi Orogenic belt (NW India) from monazite geochronology and mineral trace element geochemistry. *Lithos* **120**, 511–28.

CHOUDHARY, A. K., GOPALAN, K. & SASTRY, C. A. 1984. Present status of the geochronology of the Precambrian rocks of Rajasthan. *Tectonophysics* **105**, 131–40.

COCHERIE, A. & ALBAREDE, F. 2001. An improved U-Th-Pb age calculation for electron microprobe dating of monazite. *Geochimica et Cosmochimica Acta* **24**, 4509–22.

COGGON, R. & HOLLAND, T. J. B. 2002. Mixing properties of phengitic micas and revised garnet-phengite thermobarometers. *Journal of Metamorphic Geology* **20**, 683–96.

CONNOLLY, J. A. D. 2005. Computation of phase equilibria by linear programming: a tool for geodynamic modeling and its application to subduction zone decarbonation. *Earth and Planet Science Letters* **236**, 524–41.

CRAWFORD, A. R & COMPSTON, W. 1970. The age of the Vindhyan system of Peninsular India. *Quarterly Journal of the Geological Society, London* **125**, 351–72.

DASGUPTA, S., SENGUPTA, P., GUHA, D. & FUKUOKA, M. 1991. A refined garnet-biotite Fe-Mg exchange geothermometer and its application in amphibolites and granulites. *Contributions to Mineralogy and Petrology* **109**, 130–7.

DEB, M., THORPE, R. I., CUMMING, G. L. & WAGNER, P. A. 1989. Age, source and stratigraphic implications of Pb isotope data for conformable, sediment-hosted, base metal deposits in the Proterozoic Aravalli-Delhi orogenic belt, northwestern India. *Precambrian Research* **43**, 1–22.

DEB, M. & SARKAR, S. C. 1990. Proterozoic tectonic evolution and metallogenesis in the Aravalli-Delhi orogenic complex, northwestern India. *Precambrian Research* **46**, 115–37.

DEB, M., THORPE, R. I. & KRSTIC, D. 2002. Hindoli Group of rocks in the eastern fringe of the Aravalli–Delhi orogenic belt – Archean secondary greenstone belt or Proterozoic supracrustals? *Gondwana Research* **5**, 879–83.

DEB, M. & THORPE, R. I. 2004. Geochronological constraints in the Precambrian geology of Rajasthan and their metallogenic implications. In *Sediment-Hosted Lead–Zinc Sulphide Deposits* (eds M. Deb & W. D. Goodfellow), pp. 246–63. New Delhi: Narosa Publishing House.

ENGI, M. & WERSIN, X. 1987. Something to do with grandite garnet. SMPM.

FAREEDUDDIN, & KRÖNER, A. 1998. Single zircon age constraints on the evolution of Rajasthan granulite. In *The Indian Precambrian* (ed. B. S. Paliwal), pp. 547–56. Jodhpur: Scientific Publishers (India).

FERRY, J. M. & SPEAR, F. S. 1978. Experimental calibration of the partitioning of Fe and Mg between biotite and garnet. *Contributions to Mineralogy and Petrology* **66**, 113–17.

GOPALAN, K., MACDOUGALL, J. D., ROY, A. B. & MURLI, A. V. 1990. Sm–Nd evidence for 3.3 Ga old rocks in Rajasthan, northwestern India. *Precambrian Research* **48**, 287–97.

GOSWAMI, J. N., WIEDENBECK, M. & ROY, A. B. 1994. Single zircon ages from the Precambrian basement of the southern Aravalli Mountains (Rajasthan, India). In *Abstract 8th International Conference on Geochronology Cosmochronology and Isotope Geology* (eds M. A. Lanphere, G. B. Dalrymple & B. D. Turin), p. 115. United States Geological Survey Circular C-1107.

GREGORY, L. C., MEERT, J. G., BINGE, B., PANDIT, M. K. & TORSVIK, T. H. 2009. Paleomagnetism and geochronology of the Malani Igneous Suite, Northwest India: implications for the configuration of Rodinia and the assembly of Gondwana. *Precambrian Research* **170**, 13–26.

GUHA, D. B & GARKHAL, R. S. 1993. Early Proterozoic Aravalli metasediments and their relation with the Ahar River Granite around Udaipur, Rajasthan. *Journal of the Geological Society of India* **42**, 327–35.

GUPTA, S. N., ARORA, Y. K., MATHUR, R. K., IQBALLUDDIN, PRASAD, B., SAHAI, T., N. & SHARMA, S. B. 1980. *Lithostratigraphic Map of Aravalli Region*. Hyderabad: Geological Survey of India.

HAZARIKA, P., UPADHYAY, D. & MISHRA, B. 2013. Contrasting geochronological evolution of the Rajpura–Dariba and Rampura-Agucha metamorphosed Zn–Pb deposit, Aravalli–Delhi Belt, India. *Journal of Asian Earth Sciences* **73**, 329–39.

HENRY, D. J., GUIDOTTI, C. V. & THOMSON, J. A. 2005. The Ti-saturation surface for low-to-medium pressure metapelitic biotites: implications for geothermometry and Ti-substitution mechanisms. *American Mineralogist*, **90**, 316–28.

HERON, A. M. 1953. Geology of Central Rajputana. *Memoirs of the Geological Survey of India* **79**, 389.

HOLDAWAY, M. J. 2000. Application of new experimental and garnet Margules data to the garnet–biotite geothermometer. *American Mineralogist* **85**, 881–92.

HOLLAND, T. J. B. & POWELL, R. 1998. An internally consistent thermodynamic data set for phases of petrological interest. *Journal of Metamorphic Geology* **16**, 309–43.

HOLLAND, T. J. B. & POWELL, R. 2001. Calculation of phase relations involving haplogranitic melts using an internally consistent thermodynamic dataset. *Journal of Petrology* **42**, 673–83.

JOHNSON, T. & BROWN, M. 2004. Quantitative constraints on metamorphism in the Variscides of southern Brittany – a complementary pseudosection approach. *Journal of Petrology* **45**, 1237–59.

KAUR, P., CHAUDHRI, N., BIJU-SEKHAR, S. & YOKOYAMA, K. 2006. Electron probe micro analyser chemical zircon ages of the Khetri granitoids, Rajasthan, India: records of widespread late Palaeoproterozoic extension-related magmatism. *Current Science* **90**, 65–73.

KAUR, P., CHAUDHRI, N., RACZEK, I., KRÖNER, A. & HOFMANN, A. W. 2007. Geochemistry, zircon ages and whole-rock Nd isotopic systematics for Palaeoproterozoic A-type granitoids in the northern part of the Delhi belt, Rajasthan, NW India: implications for late Palaeoproterozoic crustal evolution of the Aravalli craton. *Geological Magazine* **144**, 361–78.

KAUR, P., CHAUDHRI, N., RACZEK, I., KRONER, A. & HOFMANN, A. W. 2009. Record of 1.82 Ga Andean-type continental arc magmatism in NE Rajasthan, India: insights from zircon and Sm–Nd ages, combined with Nd–Sr isotope geochemistry. *Gondwana Research* **16**, 56–71.

KAUR, P., CHAUDHRI, N., RACZEK, I., KRONER, A., HOFMANN, A. W. & OKRUSCH, M. 2011*a*. Zircon ages of late Palaeoproterozoic (ca. 1.72–1.70 Ga) extension-related granitoids in NE Rajasthan, India: regional and tectonic significance. *Gondwana Research* **19**, 1040–53.

KAUR, P., ZEH, A., CHAUDHRI, N., GERDES, A. & OKRUSCH, M. 2011*b*. Archaean to Palaeoproterozoic crustal evolution of the Aravalli orogen, NW India, and its hinterland: the U–Pb and Hf isotope record of detrital zircon. *Precambrian Research* **187**, 155–64.

KELSEY, D. E., WHITE, R. W., WILSON, C. J. L. & QUINN, C. D. 2003. New constraints on metamorphism in the Rauer Group, Prydz Bay, east Antarctica. *Journal of Metamorphic Geology* **21**, 739–59.

LOPEZ, R., MUKHOPADHYAY, D., BHATTACHARYYA, T. & TOBISCH, O. T. 1996. Proterozoic rim and core zircon ages for the Anasagar Gneiss, Central Rajasthan, India. *Geological Society of America, Abstract with Programs* **28**, A-492.

LUDWIG, K. R. 2001. *User Manual for Isoplot/Ex ver. 2.49. A Geochronological Toolkit for Microsoft Excel*. Berkeley Geochronological Center Special Publication 1a, 56 pp.

MACDOUGALL, J. D., GOPALAN, K., LUGMAIR, G. W. & ROY, A. B. 1983. The Banded Gneissic Complex of Rajasthan, India: early crust from a depleted mantle at ~3.5 Ga? *EOS Transactions American Geophysical Union* **64**, 351–60.

MCKENZIE, N. R., HUGHES, N. C., MYROW, P. M., BANERJEE, D. M., DEB, M. & PLANAVSKY, N. J. 2013. New age constraints for the Proterozoic Aravalli–Delhi successions of India and their implications. *Precambrian Research* **238**, 120–8.

MUKHOPADHYAY, D., BHATTACHARYYA, T., CHATTOPADHYAY, N., LOPEZ, R. & TOBISCH, O. T. 2000. Anasagar gneiss: a folded granitoid pluton in the Proterozoic South Delhi Fold Belt, central Rajasthan. *Proceedings of the Indian Academy of Sciences (Earth and Planetary Science)* **109**, 21–37.

NAHA, K. & ROY, A. B. 1983. The problem of Precambrian basement in Rajasthan, Western India. *Precambrian Research* **19**, 217–23.

NEWTON, R. C., CHARLU, T. V. & KLEPPA, O. J. 1980. Thermochemistry of the high structural state plagioclases. *Geochemica Cosmochimica Acta* **44**, 933–41.

OZHA, M. K., MISHRA, B., HAZARIKA, P., JEYAGOPAL, A. V. & YADAV, G. S. 2016. EPMA monazite geochronology of the basement and supracrustal rocks within the Pur-Banera basin, Rajasthan: evidence of Columbia breakup in northwestern India. *Journal of Asian Earth Sciences* **117**, 284–303.

PETRÍK, I. & KONEČ NÝ, P. 2009. Metasomatic replacement of inherited metamorphic monazite in a biotite-garnet granite from the Nízke Tatry Mountains, Western Carpathians, Slovakia: chemical dating and evidence for disequilibrium melting. *American Mineralogist* **94**, 957–74.

Roy, A. B. 1988. Introduction. In *Precambrian of the Aravalli Mountain, Rajasthan, India* (ed. A. B. Roy), i–viii. Memoir of the Geological Society of India 7.

Roy, A. B. 1990. Evolution of the Precambrian crust of the Aravalli Mountain range. In *Precambrian Continental Crust and its Economic Resources* (ed. S. M. Naqvi), pp. 327–48. Development in Precambrian Geology 8.

Roy, A. B. & Jakhar, S. R. 2002. *Geology of Rajasthan (Northwest India): Precambrian to Recent*. Jodhpur: Scientific Publishers (India). 421 pp.

Roy, A. B. & Kröner, A. 1996. Single zircon evaporation ages constraining the growth of the Archaean Aravalli craton, northwestern Indian Shield. *Geological Magazine* **133**, 333–42.

Roy, A. B., Kröner, A., Bhattacharya, P. K. & Rathore, S. 2005. Metamorphic evolution and zircon geochronology of early Proterozoic granulites in the Aravalli Mountains of northwestern India. *Geological Magazine* **142**, 287–302.

Roy, A. B., Kröner, A., Rathore, S., Laul, V. & Purohit, R. 2012. Tectono-metamorphic and geochronologic studies from Sandmata Complex, Northwest Indian Shield: implications on exhumation of Late-Palaeoproterozoic Granulites in an Archaean–early Palaeoproterozoic Granite–Gneiss Terrane. *Journal of the Geological Society of India* **79**, 323–34.

Roy, A. B., Somani, M. K. & Sharma, N. K. 1981. Aravalli-Pre-Aravalli relationship – a study from Bhindar, south-central Rajasthan. *Indian Journal of Earth Science* **8**, 119–30.

Saha, L., Bhowmik, S. K., Fukuoka, M. & Dasgupta, S. 2008. Contrasting episodes of regional granulite-facies metamorphism in enclaves and host gneisses from the Aravalli-Delhi Mobile Belt, NW India. *Journal of Petrology* **49**, 107–28.

Sarkar, G., Barman, T. R. & Corfu, F. 1989. Timing of continental arc-type magmatism in northwest India: evidence from U–Pb zircon geochronology. *Journal of Geology* **97**, 607–12.

Sastry, C. A. 1992. Geochronology of the Precambrian rocks from Rajasthan and northeastern Gujarat. *Special Publication of the Geological Survey of India* **25**, 96.

Sawyer, E. W. 2008. *Atlas of Migmatites*. Ottawa: NRC Research Press.

Sharma, R. S. 1995. An evolutionary model for the Precambrian crust of Rajasthan: some petrological and geochronological considerations. In *Continental Crust of Northwestern and Central India* (eds S. Sinha-Roy & K. R. Gupta), pp. 91–116. Memoir of the Geological Society of India 31.

Sinha-Roy, S. 1988. Proterozoic Wilson Cycles in Rajasthan. In *Precambrian of Aravalli Mountain, Rajasthan, India*. (ed. A. B. Roy), pp. 95–107. Memoir of the Geological Society of India 7.

Sinha-Roy, S. & Malhotra, G. 1989. Structural relations of the cover and its basement: an example from Jahazpur belt, Rajasthan. *Journal of the Geological Society of India* **34**, 233–44.

Sinha-Roy, S., Malhotra, G. & Mohanty, M. 1998. *Geology of Rajasthan*. Geological Society of India. 278 pp.

Sivaraman, T. V. & Odom, A. L. 1982. Zircon geochronology of Berach granite of Chittaurgarh, Rajasthan. *Journal of the Geological Society of India* **23**, 575–7.

Sugden, T. J., Deb, M. & Windley, B. 1990. Tectonic setting of mineralization in the Proterozoic Aravalli-Delhi orogenic belts, NW India. In *Precambrian Continental Crust and its Economic Resources* (ed. S. M. Naqvi), pp. 367–96. Development in Precambrian Geology 8.

Tiwari, H. C., Divakar rao, V., Narayana, B. L., Dixit, M. M., Madhavrao, N., Murthy, A. N. S., Rajendra prasad, B., Reddy, P. R., Venkateswarlu, N., Rao, V. V., Mishra, D. C. & Gupta, S. B. 1998. Nagaur–Jhalawar Geotransect across the Delhi/Aravalli Fold Belt in Northwest India. *Journal of the Geological Society of India* **52**, 153–62.

Tobisch, O. T., Collerson, K. D., Bhattachrya, T. & Mukhopadhyay, D. 1994.Structural relationship and Sr-Nd isotope systematics of polymetamorphic granite gneisses and granitic rocks from central Rajasthan, India – implications for the evolution of Aravalli craton. *Precambrian Research* **65**, 319–39.

Verma, P. K. 1999. Deep continental structures and processes in the Aravalli Mountain range, NW India: focus on evolution and inversion of regional faults. *Newsletters, D. S. T., Government of India* **9**, 21–4.

Verma, P. K. & Greiling, R. O. 1995. Tectonic evolution of the Aravalli orogen (NW India): an inverted Proterozoic rift basin? *Geologische Rundschau* **84**, 683–96.

Vigneresse, J. L., Barbey, P. & Cuney, M. 1996. Rheological transitions during partial melting and crystallization with application to felsic magma segregation and transfer. *Journal of Petrology* **37**, 1579–600.

Vijaya Rao, V., Rajendra Prasad, B., Reddy, P. R. & Tewari, H. C. 2000. Evolution of Proterozoic Aravalli Delhi Fold Belt in the northwestern Indian Shield from seismic studies. *Tectonophysics* **327**, 109–30.

Volpe, A. M. & Macdougall, J. D. 1990. Geochemistry and isotopic characteristics of mafic (Phulad Ophiolite) and related rocks in the Delhi Supergroup, Rajasthan, India: implications for rifting in the Proterozoic. *Precambrian Research* **48**, 167–91.

Waldbaum, D. R. & Thompson, J. B. 1968. Mixing properties of Sanidine crystalline solutions. 2. Calculations based on volume data. *American Mineralogist* **53**, 2000–15.

White, R. W., Powell, R. & Holland, T. J. B. 2001. Calculation of partial melting equilibria in the system Na_2O-CaO-K_2O-FeO-MgO-Al_2O_3-SiO_2-H_2O (NCKFMASH). *Journal of Metamorphic Geology* **19**, 139–53.

White, R. W., Powell, R. & Holland, T. J. B. 2007. Progress relating to calculation of partial melting equilibria for metapelites. *Journal of Metamorphic Geology* **25**, 511–27.

Wiedenbeck, M. & Goswami, J. N. 1994. High-precision $^{207}Pb/^{206}Pb$ zircon geochronology using a small ion microprobe. *Geochemica et Cosmochimica Acta* **58**, 2135–41.

Wiedenbeck, M., Goswami, J. N. & Roy, A. B. 1996*a*. Stabilization of the Aravalli craton of northwestern India at 2.5 Ga: an ion microprobe zircon study. *Chemical Geology* **129**, 325–40.

Wiedenbeck, M., Goswami, J. N. & Roy, A. B. 1996*b*. An ion microprobe study of single zircons from the Amet granite, Rajasthan. *Journal of the Geological Society of India* **48**, 127–37.

Appendix. Methods and data

Mineral chemical analyses (EPMA)

Major element mineral chemical analyses have been carried out with a CAMECA SX100 at the Indian Institute of Technology Bombay. Operating conditions for feldspar analyses were 15 kV with 15 nA and 15 kV, 20 nA for other minerals. ZAF corrections were applied.

XRF analyses

Bulk compositions of the samples BJ-28 and BJ-30 were determined by XRF. Analysis was done by an X-ray fluorescence spectrometer (XRF) – Bruker S8 Tiger – WD system at the Wadia Institute of Himalayan Geology, India.

Table A1. Bulk compositions (molar proportions) normalized to 100

	Pelite bulk composition (White, Powell & Holland, 2001)	BJ-28	BJ-30
Al_2O_3	38.51	36.34	30.67
FeO	29.82	21.37	50.51
MgO	15.66	16.37	12.37
CaO	1.22	6.84	3.25
Na_2O	2.44	7.92	0.37
K_2O	12.35	11.09	2.83